# Multiscale Modelling and an Experimental Investigation on Size-Scale Effects in Concrete

Simon Braun

Thesis in Partial Fulfillment for the Degree of Master of Science in Engineering

September, 2010

Department of Civil Engineering

University of Cape Town

Supervisor: Dr. S. Skatulla

Co-Supervisor: Prof. B.D. Reddy

**Abstract**

Classical continuum mechanics assumes that constitutive parameters are associated with a so-called Representative Volume Element (RVE) and are a statistical average [Mase and Mase, 1999]. This concept is based on the presumption that the specimen size is much larger than the size of its constituents, so that the behaviour of a single constituent can be neglected. This presumption does not hold true if the considered problem domain is smaller than the RVE. The size of material constituents in relation to the dimension of the specimen can then not be considered negligible and the interaction between the constituents needs to be addressed.

In this context, so-called generalised continuum formulations have proven to provide a remedy. They allow for the incorporation of internal length scale parameters which reflect the micro-structural influence to the macroscopic material response. In this way, size-scale effects of very small structures as well as heterogeneous material behaviour can be addressed in a very elegant manner.

Based on a generalised continuum framework [Sansour, 1998] a multiscale approach is proposed. A micromorphic deformation description is formulated which introduces additional degrees of freedom. The idea behind this approach is the mathematical construct of a generalised space which consists of a macrospace and multiple microspaces. The size of the microspaces is controlled by so-called internal length parameters and is each assumed to be a volume fraction of the total superimposed microspace. Making use of the micromorphic deformation description, new strain and stress measures are defined which lead to the formulation of a corresponding generalised variational principle. In contrast to classical and other generalised continuum approaches, e.g. strain gradient theories, the micromorphic approach benefits from the fact that size-scale effects can be addressed.

The outlined theory is applied to model size-scale effects exhibited in uniaxial compression experiments on concrete members. In the first, academic example, cylindrical concrete

specimens with constant specimen size but changing aggregate sizes are presented. The effect on elastic modulus due to varying model parameters is investigated.

In the second example, experimental data is captured to confirm the proposed theory and to elaborate specific values for the input parameter used to calibrate the model. The elastic Young's moduli of different sized concrete cylinders are tested and modelled. By keeping the aggregate size and its volume ratio constant, the internal length scale parameter changes with changing specimen size.

The outcome of the model and the experiments showed clearly that (i) size scale effects were captured in this specific example and (ii) by decreasing the specimen diameter, the macroscopic material stiffness increases. Furthermore, material parameter for the model are found such that the modelled results fit the experimental ones. It was expected that the magnitude of size effects levels out in larger specimens. However, this trend could not clearly be captured in the range of specimen sizes tested.

It is found that the presented micromorphic model with two micro spaces could qualitatively describe size scale effects in concrete specimens. Further experiments with a variety of different materials and a larger range of specimen sizes need to be carried out to enable prediction of the right input parameters needed for the model.

**Statement of Originality**

I know the meaning of plagiarism and declare that all the work in the document, save for that which is properly acknowledged, is my own.

I give consent to this copy of my thesis, when deposited in the University Library, being made available in all forms of media, now or hereafter known.

Signed by candidate

Student's Signature

Date

**Acknowledgements**

I deeply thank a number of people who, during the several months of this master's study, have contributed in various ways to my work.

- My supervisor, Dr. Sebastian Skatulla for his constant support and guidance throughout my research and writing that constitute this thesis. It is a great understatement to say that this work would not have been possible without his help.
- My co-supervisor, Professor Daya Reddy, who organised the funding of my studies and gave me valuable feedback on this work.
- Dr. Hans Beushausen for his critical but very helpful questions and guidance in the laboratory work.
- Noor, Charles and Lungelo for their help and corporation while casting, preparing and testing my concrete specimens.
- Muzzammil Sulaiman, who shared an office with me and was involved in many interesting late night discussions.
- My colleagues who were good buddies in our everyday life and also contributed to my work in different ways.
- My Parents, for always supporting me in my choices, making it possible for me to realise my ambitions and completing a Masters Degree abroad.
- My beloved girlfriend Robyn Williams for her emotional support, proofreading every phrase of this thesis and putting up with me during the last stages of my studies.

# Contents

# List of Figures

# List of Tables

# Notation and list of symbols

In the following the general scheme of notation and list of frequently used symbols are assembled:

$\mathbf{a}$ , $\mathbf{A}$ ..... bold roman letters denote vectors or tensors

$\mathbf{a}_{,i}$ , $\mathbf{A}_{,i}$ ..... partial derivatives of a vector or tensor quantity are denoted by subscripted primed indices

$\mathcal{A}$ ..... calligraphic upper-case letter denote sets

$\mathbb{E}(3)$ ..... three-dimensional *Euclidian* vector space

$\mathbb{R}$ ..... set of real numbers

Grad ..... gradient operator with respect to the reference configuration

Div ..... divergence operator with respect to the reference configuration

$\det(\cdot)$ ..... determinant of $(\cdot)$

Further notations, operations and relations of tensor calculus are explained as they appear in the thesis.

# Chapter 1

# Introduction and Literature Review

Classical continuum theory assumes homogeneous material behaviour in the micro-scale [Mase and Mase, 1999]. This assumption holds if the specimen is larger than the Representative Volume Element (RVE) and includes enough material constituents, e.g. grains, crystals or stones, such that the statistical average of its properties is given. The finite nature of the material constituents can then be ignored while governing and constitutive equations can be found which describe the behaviour of the specimen as a whole but also in the limit, i.e. of each infinite material point. If the specimen, however, is smaller than the RVE and the statistical average is not given, then the finite nature of material constituents must be taken into account. This is done by adding non-local information to governing and constitutive equations which address the behaviour of the constituents as a whole and its interaction with neighbouring constituents. It can be achieved by including higher gradients or degrees of freedom beyond displacements, see for example [Aifantis, 1999] or Eringen [1999]. In this sense classical theories are only accurate if the system is large enough so that the behaviour of the single constituents can be neglected. Non-classical or generalised theories that take the material's micro-structure on a kinematics level into account are characterised by degrees of freedom which go beyond classical displacement fields. Amongst those are micromorphic continua which were introduced by Ericksen and Truesdell [1957] as well as Eringen [1975]. In addition to the classical theory, the theory of micromorphic continua associates each material point with directors which describe an independent micro-displacement

field. Since the magnitude of the micro-displacement field refers to an internal length scale, micromorphic formulations can describe scale effects which relate to non-local material behaviour. Size-scale effects can be observed in uniaxial compression testing of concrete as soon as the aggregate size becomes large enough in relation to specimen size.

In this thesis, a micromorphic continuum with multiple micro-spaces is proposed in order to capture size scale-effects in uniaxial compression testing of concrete. Two micro-spaces are considered in the model to describe the material properties of aggregates and mortar matrix, respectively. The micromorphic deformation is modelled in a very general manner, opening the door for capturing scale effects in specimens experiencing no or negligible higher-order deformation gradients on the macro-scale. The approach is based on a framework introduced in [Sansour, 1998] where the generalised continuum is constructed as consisting of a macro- and micro- continuum. In this work however, the theory is extended to consider multiple micro-spaces which makes the formulation more general and accurate.

## 1.1 Literature Review

### 1.1.1 Elastic Deformation of Hardened Concrete

Concrete is a construction material produced with a large variety of different mix designs, depending on the requirements and availability of material. Correspondingly, the Young's modulus of concrete changes with every different mix design. Therefore, it is desirable to be able to estimate the Young's modulus of a concrete corresponding to its specific mix design. A very practical approach is to relate the elastic modulus and the compressive strength, since engineers usually know the compressive strength of concrete at the design stage. Many attempts have been made to correlate the Young's modulus and the strength of concrete. The South African code [SANS10100-1, 2000] uses the following equation to estimate the concrete elastic modulus at 28 days after casting:

$$E_{c,28} = K_0 + \alpha f_{cu,28}. \tag{1.1}$$

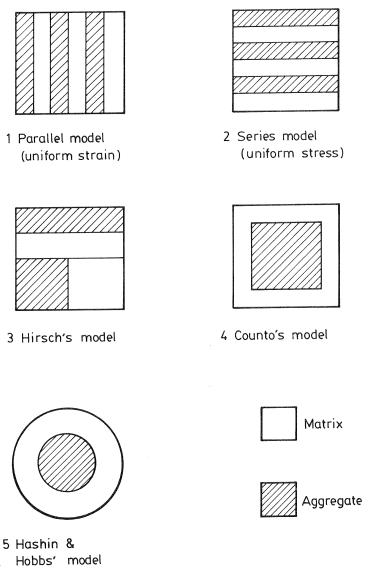


Figure 1.1: *Structural Models of Elastic Modulus for Concrete and Mortar [Alexander, 1994]*

Here $f_{cu,28}$ is the characteristic concrete cube strength at 28 days, $\alpha$ is a coefficient, and $K_0$ is an aggregate stiffness factor related to the elastic modulus of the aggregate and to its volume concentration. Local research has established various values for $\alpha$ based on specific aggregate types, whereas the South African code [SANS10100-1, 2000] specifies $\alpha$ as 0.2. Different values for $K_0$ and $\alpha$ as well as a summary of further practical approaches to estimate the elastic modulus of concrete can be found in [Alexander and Beushausen, 2009].

The overall elastic modulus of concrete can also be estimated in a more theoretical fashion. First concrete is approximated as a two-phase composite only consisting of aggregate and a cement-paste matrix. Those two individual phases are each assumed to be homogeneous and isotropic. Input parameters for those models are Young's modulus of cement-paste and aggregate as well as the volume concentration of aggregate. Figure 1.1 summarises a number of two-phase composite models. The Parallel model assumes uniform strain and the Series model assumes uniform stress, which set the upper and lower bounds respectively. Neither of these models describe reality precisely, since concrete experiences neither uniform strain nor uniform stress under compression. Models 3 to 5 are more realistic and the corresponding values of the overall Young's moduli lie in between the first two models. Figure 1.2 compares the values of the presented two-phase models. It can clearly be seen that

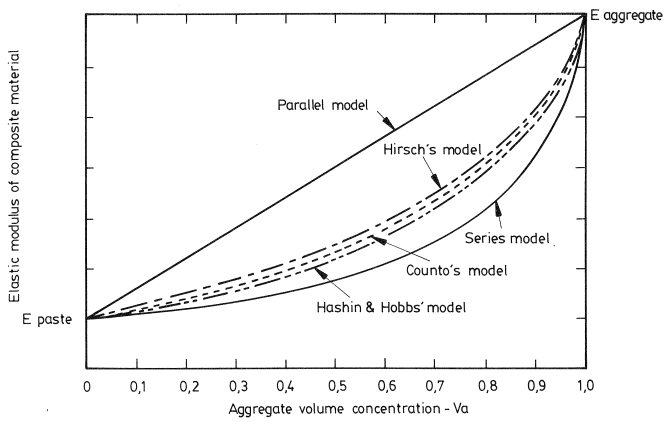


Figure 1.2: *Comparison of Structural Models of Elastic Modulus for Concrete and Mortar [Alexander, 1994]*

in all models (except the Parallel model) the overall stiffness is mainly dependent on the weaker phase, i.e. the cement-paste. The formulae of all models as well as the corresponding references can be found in [Alexander, 1994].

Even though the presented two-phase models provide reasonably good approximations to the mechanical behaviour of concrete, they all neglect the influence of the interface layer between aggregate and cement, called the interfacial transition zone (ITZ). The ITZ is a thin layer around the aggregates which is more porous than the bulk of the surrounding cement-paste matrix. The size of cement grains ranges from less than one micron to up to 100 microns [Scrivener et al., 2004]. Compared to the cement grains, the size of the aggregate is several orders of magnitude larger. The aggregates can therefore be seen as a wall which disrupts the packing of the cement grains. If a wall would be placed into a random assembly of cement grains, it would cut through some grains as shown in Figure 1.3A. As this is physically impossible, the larger grains are forced away from the wall (Figure 1.3B). This so called *wall effect* is the main reason for the existence of ITZ [Scrivener et al., 2004]. There are no discrete boundaries between the ITZ and the bulk paste, but the thickness of the ITZ depends on the maximum cement grain size. The thickness of the ITZ has been estimated to be between 15 and 40 $\mu$m [Hashin and Monteiro, 2002]. Particles of silica fume ranging in size down to about 0.1 $\mu$m. Adding silica fume to the cement-paste therefore allows a better packing of the grains and thus reduces the effects of the ITZ [Scrivener et al., 2004].

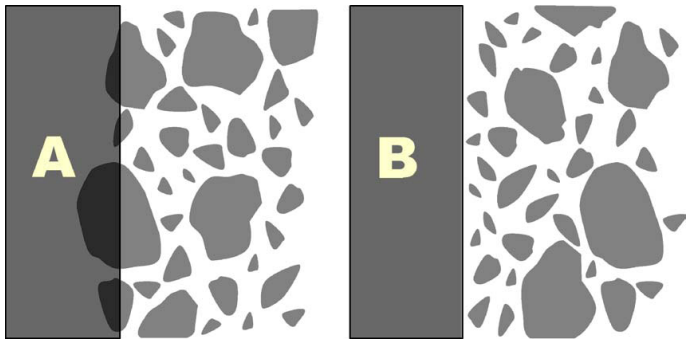


Figure 1.3: *Wall Effect [Scrivener et al., 2004]*

The generally higher porosity in the ITZ also leads to a locally higher water to cement (w/c) ratio. As the Elastic modulus of the cement-paste is directly influenced by the w/c ratio, it can be concluded that the ITZ zone is weaker than the bulk paste. It was estimated that the elastic modulus of the ITZ is about 30-50% of the bulk paste [Lutz et al., 1997]. Since the total amount of water is constant, the w/c ratio in the bulk paste must automatically be reduced [Scrivener et al., 2004]. This indicates that the elastic modulus of the bulk paste must be slightly stiffer than that of a bulk paste in a specimen without aggregates (ITZ).

Simeonov and Ahmad [1995] showed by means of experimental data that the elastic moduli of concrete are intimately related to the elastic moduli and volume fraction of the ITZ. Thus, when modeling the Young's modulus of concrete based on its microstructure, it is important to consider concrete as a three-phase composite consisting of aggregates, the ITZ and bulk paste matrix [Nilsen and Monteiro, 1993]. Numerous authors present a large variety of different three-phase composite models to estimate the overall Young's modulus of concrete or mortar. Zhao and Chen [1998] derive engineering formulas by simply expanding model 1 and 2 (Fig. 1.1) by a third phase and taking the logarithmic weighting average of those two formulae. They also find that the elastic modulus of concrete is not sensitive to changes of local geometrical and physical quantities relating to a small region in a body. If the shape of an aggregate changes from circular to square or quadrilateral, the change in the overall elastic modulus is negligible as long as the volume ratio of the aggregates does not change. Nadeau [2003] developed a self-consistent effective-medium theory to calculate the overall predictions for mortar and concrete elastic moduli. In his theory, Nadeau incorporates the

w/c ratio gradients throughout the ITZ. He found that the overall w/c ratio given by the mix design must be conserved in the microstructure. Sun et al. [2007] improved Nadeau's work by making accurate experimental measurements and using a differential effective-medium theory. They believe that this theory is more suited to concrete microstructure than self-consistent effective-medium theories, as it better matches the actual concrete microstructure consisting of generally non-touching aggregates in a cement-paste matrix. Sun and his co-workers consider concrete as consisting of a matrix material containing effective inclusions. Each particle surrounded by a shell of ITZ is first mapped onto an effective particle with uniform elastic moduli. The resulting matrix material and effective particle is then treated as a two-phase composite.

More recently, Lee and Park [2008] presented a numerical concrete model which adopts the three-phase model and uses the finite element method with material discontinuities. In conventional finite element analysis of composite materials each element can only be endowed with a single material. Hence, meshing concrete precisely in three dimensions and incorporating the ITZ becomes very difficult. To overcome these shortcomings, Lee and Park adopted the numerical integration method which accurately calculates the stiffness of uniform finite elements with material discontinuities.

### 1.1.2 Representative Volume Element

The previously mentioned models all seek to derive information on the overall, constitutive behaviour. The generally complex and strongly heterogeneous material properties on a microscopic level are considered to result in homogeneous material behaviour on a macroscopic level. However, all those models are only valid if the considered problem domain, e.g. the specimen size, is larger than the Representative Volume Element (RVE). The RVE can be defined as the smallest material volume element which, when translated through the heterogeneous material, does not change its statistical properties [Bažant et al., 2004]. Therefore, in order to represent an accurate mean constitutive response, the RVE must include a sufficiently large number of the material's micro-heterogeneities such as grains, inclusions, voids, cracks, fibres, etc. This is a rather qualitative definition, because it does not clearly define

'statistical properties' nor what constitutes a 'sufficiently large number'. There is much confusion and many different opinions in the literature on the determination of the RVE's size. Lemaitre [1987], for example, suggested that the minimum RVE size should be around 0.1 mm for metallic materials, 1 mm for polymers and composites, 10 mm for woods and 100 mm for concrete. However, these specifications are related to damage mechanics where the scale to be considered is much larger than the one for conventional elasticity or plasticity. Wang et al. [2002] determined the RVE size for a fractured rock mass to be 15 m. Generally, one relates the minimum required RVE size to the size of the maximum size of inclusions. Drugan and Willis [1996] showed that for a maximum error of 5 % of the constant overall modulus in elastic fibre composites, the minimum RVE size is at most twice the inclusion diameter. Even for higher accuracy - a maximum error of 1 % - the minimum RVE size lies at around 4.5 times the fibre reinforcement diameters. van Mier and van Vliet [2003] suggest that the minimum ratio between maximum aggregate size and the specimen dimension should be larger than 8 for concrete specimen subjected to uniaxial tension. In a recent study, Xu and Chen [2009] suggest based on a numerical characterization, that for three-dimensional problems the size threshold of the minimum RVE size is approximately between 10 and 20 times of the inclusion diameter, based on a range of accuracy criteria between an error of 1 % and 0.1 % respectively.

### 1.1.3 Size Scale Effects

Any specimen with materials containing grains or inclusions can be classified with an internal length scale parameter. The internal length scale parameter refers usually to the size of the material's micro-structure, i.e. the size of the grains or inclusions. If the specimen size is large enough, i.e. it fulfills the criteria of the RVE, a change in the internal length scale parameter should not affect the overall or effective material properties of the test specimen. However, if the specimen is smaller than the material's RVE, the material properties of the specimen, for example Young's modulus, may vary with respect to the effective properties. This change in material properties, i.e. a change in the specimen size to aggregate size ratio, is generally referred as size scale effects.

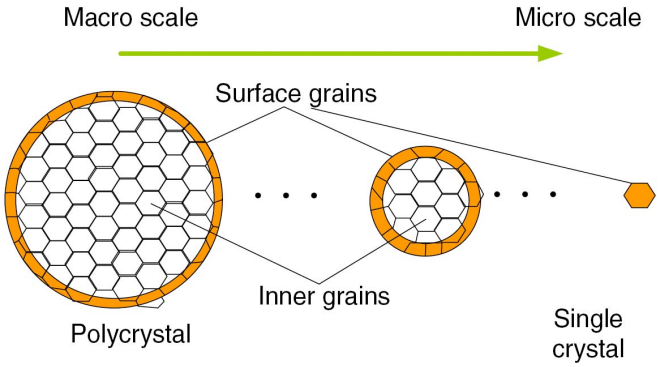


Figure 1.4: *Grain Distribution in a Material Section with the Decreasing of the Feature Size [Lai et al., 2008]*

In the process of sheet metal working, for example, it is important to take size effects into account. In recent years there has been a growing demand for mechanical micro-parts; for products ranging from mobile phones and computers to medical products [Engel and Eckstein, 2002], [Peng et al., 2007]. When the feature size of micro-parts is reduced to smaller than 1 mm, the material behaviour can then differ from that in the macro-scale. Looking at a thin metal sheet, the material behaviour is characterized by only a few grains located in the deformed area. Thus, the material can no longer be considered as a classical continuum, because the overall behaviour actually depends on the properties of the single grains. Lai et al. [2008] show that size effects are influenced by the grain size, grain orientation and feature size. Mahabunphachai and Koç [2008] show that the specimen size effect has substantial impact on the material response as the feature or specimen size reduces to the micro-scales. Tensile tests showed that as the specimen size decreases, so does the corresponding flow stress. The flow stress is a common parameter to describe the plastic deformation behaviour of materials. Engel and Eckstein [2002] and Michel and Picart [2003] report similar observations of this trend of decreasing flow stress with decreasing specimen size and explained it with the so-called surface model. The surface model states that the grains inside a specimen are more restricted than the grains located on the free surface. This leads to less hardening and lower resistance to deformation of surface grains and thus makes them weaker. The proportion of the surface grains to the inner grains rises with the minimization of the specimens as illustrated in Figure 1.4. This explains the scaling effects

occurring in the micro-scale and why smaller specimens generally have a lower flow stress.

Size effects can also be found in concrete structures. Vořechovský [2007] proposes that size effects in concrete specimens under tension are predominantly caused by the randomness of local material strength. Aggregates, the ITZ and cement-paste have a certain mean strength and standard deviation. Specimens with larger aggregates are more heterogeneous and test results are therefore expected to vary more. Vořechovský [2007] showed by means of a stochastic model that specimens with small grains fail sooner than specimens with larger grains. This can be explained because the chance that the specimen contains a weak link is higher in both specimens with small aggregates or in large specimens.

Another plausible explanation for size scale effects in concrete is that concrete specimens contain a weaker surface layer due to drying of concrete. Drying of concrete produces large self-equilibrated stresses in the cross-sections of concrete structures. As argued in [Bažant et al., 2004], at the beginning of drying, the surface layer of load-free specimens is in tension and undergoes micro-cracking. The depth of penetration of a drying front into a wall is roughly proportional to $\sqrt{t}$ where $t$ is the drying time. Small specimens are more affected by drying and are thus weaker. Large specimens are usually not affected by drying since the surface layer is only a small proportion of the whole cross-section.

van Mier and van Vliet [2003] show that size effects can also be caused by particle packing. Ideally the aggregates of each size should randomly be placed throughout the specimen volume. This is not always the case, as the heavier parts of fresh concrete sink to the bottom of the specimen, see Figure 1.5. The material composition and therefore the mechanical properties differ from top to bottom of the specimen. Due to the wall effect, only small aggregates can be placed close to the walls of the mould as can be seen in Figure 1.5. A layer close to the surface therefore contains smaller grains on average than the concrete inside a specimen. The volume fraction of aggregates to cement-paste is therefore also smaller. The thickness of this layer is dependent on the maximum grain size.

The last type of size scale effects discussed in this literature review is the influence of non-local stress. Classical continuum theories lack the capability of representing size scale effects since they do not incorporate an internal length scale parameter. Several modifications

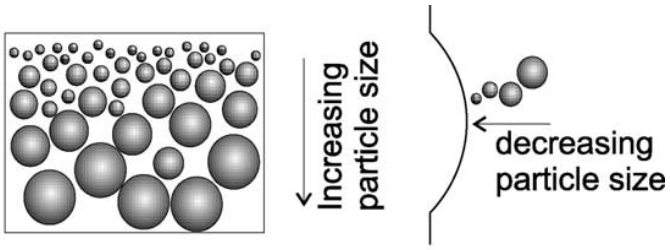


Figure 1.5: *Particle Packing, Segregation and Wall Effect [van Mier and van Vliet, 2003]*

have been proposed to overcome this issue. A big contribution to the development of non-local theories of linear and non-linear elasticity has been given by Eringen ([Eringen and Edelen, 1972] and [Eringen, 1981]). Aifantis and his co-workers address size scale effects by means of a strain-gradient approach in numerous publications, see for example [Aifantis, 1999]. Further development in this field has been done by Fleck and Hutchinson [2001]. Lam et al. [2003] developed a strain-gradient elastic bending theory for plane-strain beams. They observed size-scale effects in experimental testing on micron-sized isotropic elastic cantilever epoxy beams. The material strength increased with decreasing beam thickness. This effect was in good agreement with their proposed model. Their results showed the significance of the elastic strain gradient effects in small-scale structures. The predictions of non-local stress approaches usually reduce to those of classical continuum theories as the specimen size becomes much larger than its internal length scale.

### 1.1.4 Generalised Continuum Theories

Non-classical or generalised theories, which take a material's micro-structure into account, are characterised by degrees of freedom which go beyond classical displacement fields or higher order displacement gradients. Micromorphic continua were first introduced by Ericksen and Truesdell [1957] as well as Eringen [1975]. In addition to the classical theory, micromorphic continua associates each material point with directors which describe an independent micro-displacement field. Since the magnitude of the micro-displacement field refers to an internal length scale, micromorphic formulations can describe scale effects which relate to non-local material behaviour. The micromorphic continuum theory can be differentiated

into Micropolar -, Microstretch - and Micromorphic continua.

The *Micropolar* continuum theory can be seen as the simplest case of the non-classical or the so-called generalized continuum theory. In addition to the classical theory, each material point is associated with three orthogonal directors which describe a rotation field that is independent of the conventional displacement field. The directors are rigid and the material particles can translate and independently rotate. Every material point contains six degrees of freedom; the three classical ones which describe the translational motion in the macro space and additional three which refer the rotation around the three macro-coordinate axes in the micro-space. The theory can be used to describe liquid crystals or animal blood with rigid cells, for example [Eringen, 1999]. In this case, the blood would represent the macro-space whereas the rigid and incompressible cells would represent the micro-space. The invention has been done by the Cosserat brothers in 1909 and is therefore also known as *Cosserat* continua. Further work and summaries of the micropolar continuum theory has been done by [Mindlin, 1964], [Eringen, 1999] or [Ramezani and Naghdabadi, 2007]. Applications of the micropolar continuum theory include modeling thin elastic shells [Altay and Dökmeci, 2006] or analyzing elastic beams [Ramezani et al., 2009].

The *Microstretch* continuum theory is a generalisation of the Micropolar continuum theory which was mainly developed by A.C. Eringen in the 1970's. In the Micropolar theory, the micro continua possesses internal expansion and contraction modes, in addition to micropolar modes. In this theory, not only can the directors translate and rotate, they can also also stretch and contract. There are in total seven degrees of freedom; three classical ones, three for the microrotation and one for the microstretch [Eringen, 1999]. This theory can describe micro-deformation more accurately and finds its application in composite materials and various porous media. The microstretch continuum theory was applied, for example, to model the thermal stresses in elastic plates [Leşan and Quintanilla, 2005].

Although the *Micromorphic* continuum theory is the least developed field, it is the most generalised approach. The theory was also introduced by A.C. Eringen in the 1970's. It is the most generalised formulation and it includes micro-rotation, micro-stretch and micro-shearing [Eringen, 1999]. Every material point is associated with free deformable

directors. If the micro-space is three-dimensional, the formulation has nine or more extra degrees of freedom over the classical theory. Application of this theory is sparsely found in literature, because it is a relatively new research area. However, Lee and Chen [2004] used the micromorphic theory to study electromagnetic wave propagations in micromorphic elastic solids due to external loads of thermomechanical and electromagnetic origins. In 2006, Dillard et al. [2006] used an anisotropic compressible plasticity model incorporated into the framework of the micromorphic continuum theory in order to model deformation and fracture behaviour of nickel foams. Such metallic foams are strongly heterogeneous materials and therefore prone to exhibit size effects in their mechanical behaviour. Dillard et al. [2006] showed that the micromorphic continuum theory is an appropriate and accurate way of describing such heterogeneous materials.

### 1.1.5 Meshfree Modelling

In order to solve any of the previously mentioned continuum models, the use of computer technology is essential. The finite element (FE) method is generally very powerful and is normally the first choice to model formulations of solids and structures. In the FE method the body is divided into a number of finite elements. After the governing equations are described and appropriate boundary conditions are set, a solution for every nodal point can be obtained using approximation techniques. The accuracy of the FE method solution is strongly dependent on the mesh size. By refining the mesh size, the approximated solution converges to an exact solution. The following books are recommended for further reading about the finite element method [Hughes, 2000] and [Zienkiewicz and Taylor, 2005].

The FE method has found wide applications in classical continuum formulations. Nevertheless, next to the classical ones, the FE method has also been successfully used to model non-classical formulations. Dillard et al. [2006], for example, implemented a two-dimensional FE model with six independent degrees of freedom, to model size scale effects of nickel foam. Another example where the FE method was used in a rather exotic field is the work done by McVeigh and Liu [2008]. They developed a multi-resolution continuum theory in order to predict material response in material with inhomogeneous deformation at multiple scales.

The resulting multiresolution finite element theory was used to model ductile failure in a steel alloy, brittle-ductile failure in cemented carbide and adiabatic shear band propagation in steel alloys.

However, depending on the problem that needs to be solved, the FE method is not always the best choice, because it is rather limited in terms of implementation. Xia and Hutchinson [1996] used FEM to calculate plane strain crack tip fields in strain gradient plasticity. They, however, reported some difficulties at arriving at an accurate numerical scheme, when strain gradients come into effect. Zervos et al. [2001] modeled localisation and scale effects on thick-walled cylinders based on a second-gradient elastoplastic model. For the numerical implementation, they used a finite element displacement formulation with continuously differentiable functions. However, the implementation led to a very large number of nodal degrees of freedom which result in large calculation costs.

Those difficulties and inconveniences, amongst others, led to the development of several so-called meshless methods in the last few decades. These methods are more flexible and contain possibilities which go beyond those of the classical FE method. It is possible to deal with large deformations, changing domain geometry or necessitated higher-order-approximation continuity. The essential difference to the FE method is that meshless methods do not require a rigid mesh because the approximation is constructed entirely in terms of nodes [Belytschko et al., 1996]. Meshless methods opened the door to solve large classes of problems. The following section shows a brief overview on the most important methods.

The starting point of meshless methods was the *Smooth Particle* (SPH) method developed around 30 years ago which dealt with the strong form of the partial differential equations. Lucy [1977] and Gingold and Monaghan [1977] developed the SPH method and modelled astrophysical phenomena without boundaries like exploding stars or dust clouds.

Another method of constructing meshless approximations is the use of Moving Least Square (MLS) approximations. Nayroles et al. [1992] used MLS approximations in a Galerkin method called the *Diffuse Element Method* (DEM). The DEM can be seen as a generalization of the widely used FE method. It presents several advantages when compared to the FE method, specially for evaluating the derivatives of the unknown functions. However, it

was recognised that the precision and the convergence rate of the DEM was quite poor in comparison to the finite element method.

Belytschko and his co-workers developed the *Element-Free Galerkin* (EFG) method which is a modification of the DEM method. With some improvements in the implementation, they proposed to achieve an increased accuracy, no volumetric locking and a higher rate of convergence than the DEM and FE method. The method is applicable to arbitrary shapes but requires only nodal data. Belytschko et al. [1994b] applied this method to elasticity and heat conduction problems. It has also been proposed that this method is suitable for the modelling of the propagation of cracks, since it requires hardly any remeshing [Belytschko et al., 1994a]. In a finite element context, an alternative to remeshing is the *Extended Finite Element Method* (XFEM) [Belytschko and Black, 1999]. Enrichment functions which contain a discontinous displacement field are added to the finite element approximation. The method can solve most crack growth problems without any remeshing or with some remeshing near the crack root. The XFEM exploits the partition of unity property of finite elements, which allows local enrichment functions to be easily incorporated into a FE approximation [Moës et al., 1999]. Bordas and Duflot [2007] reported that the extended finite element method lacks on smoothness of the resulting derivatives. A further drawback of the XFEM as well as the FE method is that they cannot deal with distorted meshes very well, which decreases their direct applicability to problems involving high mesh distortion [Nguyen et al., 2008].

The *hp-clouds* method was developed by Duarte and Oden [1996]. The hp-clouds method is extrinsic, because it contains both high-order monomials and enhancement functions as well. The use of enhancement functions led to an improvement in the approximation performance. Babuška und Melenk discovered the similarities of meshless and FE methods and developed the so-called *Partition of Unity Method* (PUM) which is similar to the hp-cloud method [Babuška and Melenk, 1997]. The PUM method has high flexibility in the choice of the local approximation.

For further information regarding the huge variety of the meshless methods, refer to [Belytschko et al., 1996] and [Nguyen et al., 2008]. Those works provide a thorough study and comparison between the aforementioned meshless methods.

## 1.2 Research Motivation

### 1.2.1 Problem Definition

Several approaches of how to estimate the elastic Young's modulus of concrete can be found in literature. More general models which predict the overall Young's modulus of two-phase and three-phase composites are also available. The stiffness of concrete can be correlated with its compressive strength [SANS10100-1, 2000] or it can simply be computed, if information of the stiffness of its individual composites is known [Alexander, 1994]. Formulations have been proposed that take into account water to cement ratio gradients and the corresponding change in stiffness within the ITZ and in the bulk paste [Nadeau, 2003]. Most recently, a numerical concrete model which adopts a three-phase model and uses the finite element method with material discontinuity has been proposed [Lee and Park, 2008].

These different approaches in estimating the elastic modulus of concrete do not take into account the ratio of aggregate size and specimen size. There is literature that considers size scale effects in fracture mechanics of concrete. However, no research as yet has been done on size effects in the elastic regime of concrete, i.e. before micro-cracking occurs.

Size effects occur as soon as the considered problem domain becomes smaller than the Representative Volume Element (RVE). Knowledge of the size of a materials RVE is important in order to know whether a classical theory is valid or if non-local contributions have to be considered. Many suggestions have been made on the size of the RVE, but there is still much confusion about exact specifications of the RVE size of concrete.

### 1.2.2 Research Aims

A micromorphic continuum theory with multiple micro-spaces is proposed in the current research study. Non-local information is added to governing and constitutive equations which address the material's micro-structure. The micromorphic deformation is modelled in a very general manner, opening the door for capturing size scale effects in uniaxial compression testing of concrete. The aims of this study are modelling size scale effects, capturing its

magnitude at a given range of specimen sizes and obtaining an indication of the RVE size of concrete.

The outlined theory is implemented in a numerical computer programme which, contains calibration factors. It is expected that by decreasing the specimen size, the material generally becomes stiffer. Experiments are carried out to confirm this trend and to obtain values for the calibration parameters.

### 1.2.3 Scope of Research and Limitations

Part of this work includes extending the current model [Sansour et al., 2010] with a second micro-space. The code is written in the object-oriented C++ programming language which makes it easy to structure and extend the code. In order to utilise a supercomputer with a distributed memory architecture, the coding is parallelised making use of the so-called *message parsing interface* (MPI).

In the second phase, an academic example is outlined to show the applicability of the introduced micromorphic multiscale formulation, and to qualitatively display size scale effects in concrete specimens. Simulations with different values for the introduced calibration parameters are performed to demonstrate the flexibility of the coding.

The theory is confirmed by means of experiments. Concrete specimens of different sizes are produced, tested and evaluated. Finally, the experimental results are used to find specific values for the as yet unknown material parameters.

The range of specimen sizes is limited to the core diameters of the drill used to core the specimens. The smallest core diameter available in the concrete lab is 22.5 mm and the largest available diameter is 100 mm. In order to cover a maximum ratio of specimen size to aggregate size, specimens with two different aggregate sizes were cast, namely 6.7 mm and 26.5 mm. The accuracy of the computer simulations is limited by the choice of quadrature order and the number of integration points. The accuracy of the experimental test results is limited by the accuracy of the relevant testing machine and the number of test specimens. The number of test specimens of each size was chosen to be four. By the determination of

the specimen's Young's modulus, the strain readings were taken on two opposite sides of the specimen.

## 1.3 Overview of Thesis Structure

The organisation of this Thesis is as follows. The next chapter provides a brief overview on concrete technology. In Chapter 3, fundamentals of the classical continuum theory are outlined and in the subsequent Chapter 4, the theory of the generalised continuum with its corresponding variational principle is proposed. Chapter 5 gives insight into some of the most important modelling related aspects of the current research project. The capability of the proposed theory and the flexibility of the implemented model are demonstrated in a theoretical example in Chapter 6. Finally, in Chapter 7, the theory is confirmed by means of experiments and the model is calibrated based on the obtained experimental data.

# Chapter 2

# Concrete Technology

The following chapter provides a very brief overview of the concrete technology required for a basic understanding of the experiment presented in this thesis. If not otherwise stated, all the information in this chapter was taken from Addis [2007]. For any further and more specific information on concrete and its behaviour, the reader is also referred to Owens [2009]. Note that long term effects such as durability or creep have been omitted, since they are not relevant for the current study. However, information about those topics can be found in the aforementioned references.

## 2.1 Concrete Material Constituents

Concrete is essentially made of aggregates, cement and water. Many different aggregates are used for the production of concrete, based on the availability of local materials, cost and requirements of concrete. The following sections provides a brief overview of the different material and their characteristics.

### 2.1.1 Cement

Cement is a fine mineral powder that reacts chemically when mixed with water. The mix is initially soft but after a few hours, it sets and hardens to a rigid mass. This time is essential

to provide the time to transport, place and compact concrete, before it sets. The setting of cement is caused by hydration which is a chemical reaction between the cement and water. The rate of hydration is not uniform. Initially, the strength increases rapidly and slows down with time.

A commonly used cement in South Africa is Portland cement. Portland cement is produced by grinding limestone and clay to a fine powder, blending it together and heating the mixture in a cement kiln up to a temperature of 1450 °C. By heating this blend, calcium, silicon, aluminum and iron react and form cement clinker. Portland cement is the result of finely ground cement clinker with a small amount of gypsum.

Cement can be used in combination with so called cement extenders. These products are usually industrial waste products which reduces the cost of concrete but can also enhance the durability of cement. Furthermore, if they are not recycled in this way, they harm the environment. It is important to note that extenders can only be used in combination with cement, never on its own. Fly ash for example, is a by-product of coal fired power stations. Adding silica fume to the mix design of concrete improves the workability and enhances the durability. Due to its very fine grain sizes it fills the pores closer to the aggregates which reduces the adverse effects of the ITZ. Other extenders used in South africa include condensed silica fume and ground granulated blastfurnace slag.

### 2.1.2 Aggregates

Aggregates, normally derived from rock, are important constituents of concrete. Adding aggregates to concrete is mainly done to reduce the cost and improve the dimensional stability of the hardened concrete. Aggregates make up to 70 % of the volume of concrete and are divided into *fine aggregates* (sand) and *coarse aggregates* (stones). Sand is defined as particles that pass through a sieve with 4.75 mm square openingsconstitutents. Stone particles are larger, i.e. those that do not pass through this sieve.

Aggregates should be clean, hard, strong, dimensionally stable, durable and free from any clay coatings or organic materials. Aggregates can be characterised by grading, fines

modulus, bulk density, particle relative density, particle shape, surface texture, strength, shrinkage and geological type and source. In South Africa, stones are usually manufactured by crushing rock, whereas sand is taken from rivers, pits, beaches and deserts. Aggregates from different sources have different characteristics which eventually influence the workability of fresh concrete as well as the properties of hardened concrete. Usually, it is desirable to use locally available aggregates to avoid lengthy transportation periods.

### 2.1.3 Water and Admixtures

Water has two roles in concrete; it makes fresh concrete workable and it reacts with cement. Water used for making concrete should be fit to drink. Therefore, any water taken from municipal sources is suitable. Sea water may also be used in unreinforced concrete where efflorescence or mottling does not matter and aggregates are not liable to be attacked by the alkalis in the water.

Admixtures are substances added to concrete at the mixing stage to modify some of the properties of concrete. Admixture types include plasticizers, superplasticizers, air entrainers, accelerators and retarders. To decrease the water to cement ratio plasticizers are used. This results in higher compressive strength of hardened concrete. Plasticizers also make the concrete more workable and hence they are used to decrease material cost by using less cement. Superplasticizers react in the same as plasticizers, but the effect is about three times greater. Air entrainers introduce small amounts of air bubbles in concrete which increases the workability and improves resistance to frost damage. Accelerators increase the rate of hydration of cement. They can be used either to accelerate the strength-gain or the setting-time. Retarders delay the setting of concrete and are used if concrete has to be transported for a long time.

## 2.2 Properties of Fresh Concrete

Concrete is considered as *fresh concrete* from the time it is mixed until it sets. In this time the concrete is handled, transported, placed and compacted. Even though the fresh state lasts only a few hours, its properties are important, because they influence the quality of the hardened concrete. Important properties of fresh concrete include consistence, workability, settlement and bleeding, and plastic shrinkage.

*Consistence* is a measurement of the stiffness/sloppiness or fluidity. It is important that the consistence is the same for each batch for effective handling, placing and compacting of the concrete. Consistence of conventional concrete is usually measured with the slump test as described in the South African code [SANS5862-1, 2006].

*Workability* is defined as the relative ease with which concrete can be placed, compacted and finished without separation or segregation of the individual materials. It must be noted that workability is not the same as consistence; mixes with the same consistence can have different workabilities, if they are made with different aggregate sizes for example. Workability can not be measured, but a useful indication can be obtained by the slump test together with an assessment of properties. The major influences of workability are aggregate size, fines content of sand, cement and stone content.

Due to different densities, cement and aggregates tend to settle down while the mixing water migrates and moves upwards. This effect is referred as *settlement and bleeding* and it continues until the concrete sets. Bleeding can be beneficial, because it reduces the w/c ratio and thus improves the strength of the concrete. However, bleeding should be avoided, because voids and weak internal surfaces are created and it increases permeability of the hardened concrete. Furthermore, concrete may crack at places where settlement is restrained, ie. by horizontal reinforcement. Bleeding is commonly reduced in practice by adding fine material in the mix such as silica fume.

*Plastic Shrinkage* is caused by removal of water from the fresh concrete which leads to a reduction in volume of the concrete. Plastic shrinkage is not harmful in itself, but if the shrinkage is restrained, it may cause the concrete to crack. Exposure to direct sun, high

ambient temperatures and wind increases the evaporation from the surface of the concrete. Shrinkage is usually prevented by covering the concrete surfaces with plastic sheeting.

## 2.3 Properties of Hardened Concrete

Once fresh concrete has set and hardened, strength is the most important property of concrete. Concrete without high strength is mostly useless, but concrete which is unnecessarily strong is not economical. In order to produce concrete with the desirable strength, measuring methods are necessary.

There are three different types of concrete strengths that can be measured, i.e. compressive strength, tensile strength and bond strength. Compressive strength tests are applied in practice, whereas the other two are more theoretical. A commonly used method to measure compressive strength of concrete is by testing concrete cubes. Concrete is cast in cube moulds and the specimens are usually crushed 28 days after casting. The required steps for the compression test are outlined in Section 7.1.4. The monitored failure load $F$ is then used to calculate the maximum compressive load

$$f_c = \frac{F}{A} \tag{2.1}$$

where $f_c$ is the compressive strength in $N/mm^2$ and $A$ is the cross sectional area of the specimen in $mm^2$. Note that the cross sectional area is measured in its undeformed state. The strength of concrete is also often measured in Megapascals where $1MPa = 1N/mm^2$. The tensile strength tests are usually carried out by either flexure or splitting. Concrete is much stronger when loaded under compression than under tension. There is no general relationship between compressive and tensile strength, but for conventional concrete, one could expect that the tensile strength is roughly 10 % of the compressive strength. The bond strength only applies for reinforced concrete, where round steel bars are embedded in the concrete. Bond strength offers resistance against movement of the reinforcing bars and is a combination of the effects of adhesion, friction and shear.

Concrete will always fail under tension due to its much smaller tensile strength. Even if a specimen is subjected to only compression, the material will expand which leads to tension cracks parallel to the applied load. Concrete can therefore be seen as a chain consisting of three links: aggregates, cement paste and the interfacial transition zone (ITZ). The maximum strength of concrete is reached when the weakest of these links fails. In conventional concrete, aggregate strength has no significant influence, since it is much higher than the other two links. The strength of hardened cement paste and of the ITZ influences the concrete strength. The strength increases with decreasing w/c ratio and increasing age. Furthermore, the bond of aggregate and cement paste increases with reduced bleeding and increasing roughness of aggregate surfaces.

The compressive strength of concrete also depends on how the concrete is tested. Standard cube specimens loaded at right angles to the direction of casting are on average about 5 % weaker than those loaded parallel. This effect is caused by the existence of lens shaped voids under the aggregate particles due to bleeding and settlement. The specimen geometry and size also influences the compressive strength. The compressive strength decreases as specimen size increases; 200 mm cubes are about 10 % weaker than 100 mm cubes. Cylindrical specimens with height that is double its diameter are about 15 % weaker than if the height and diameter are the same. Possible explanations of these geometry and size dependent variations of concrete stiffness are part of this research project and will be discussed later.

Any concrete structure undergoes deformation which can be divided into elastic, creep and shrinkage. If, for example, a concrete column is subjected to a load it deforms immediately which is referred to an *elastic* deformation. The column, however, also deforms gradually in time which is called *creep*. The third type of deformation, called *drying shrinkage*, is also a long term effect and is due to a gradual loss of moisture to its environment. Shrinkage differs to the other two types of deformation in that it is independent of the loading of a structure.

When a load is applied to any structural material it deforms in a certain way. If, upon removal of the applied load, the material returns to its original shape, one talks about

perfectly elastic material behaviour. Furthermore, if the relationship of deformation to applied load is linear, i.e. a straight line on a stress strain curve, the material is considered linear elastic and can be approximated with the well known Hooke's law

$$\sigma = E * \varepsilon \tag{2.2}$$

where $\sigma$ and $\varepsilon$ are the one-dimensional stress and strain respectively, and $E$ is a constant called modulus of elasticity or Young's modulus. When the deformation behaviour of a material is plotted on a stress-strain curve, the Young's modulus represents the slope of the obtained curve.

The Young's modulus for every material is unique and is captured by experiments for common materials. Most construction steels, for example, are considered as linear elastic in a range below yielding. The stress-strain relationship for concrete however is not constant or linear, i.e. it does not obey Hooke's law [Alexander and Beushausen, 2009]. The slope of a stress strain curve decreases with increasing strain. This non-linearity is mainly due to the non-linear stress-strain response of the paste and to micro-cracking in the matrix. However, the Young's modulus of concrete can be approximated as linear in the first 30 % to 40 % of ultimate failure load. This first part of the curve is referred as *Initial Tangent Modulus* as shown in Figure 2.1. Note that the behaviour of concrete is only considered elastic when

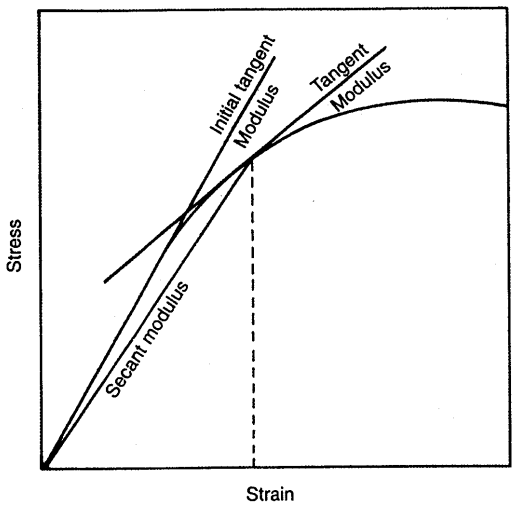


Figure 2.1: *Stress vs. Strain for Short-term Loading of Concrete [Addis, 2007]*

the specimen is loaded for a short time.

The Young's modulus of concrete can be measured by means of static and dynamic tests. In static tests a concrete specimen is uniaxially loaded and its deformation is measured. The exact procedure is described in Section 7.1.5. In dynamic tests, the specimen is excited with a variable-frequency oscillator and the Young's Modulus can be derived from the frequency at which the specimen resonates.

The major factors influencing the Young's modulus of concrete are the stiffness of the paste phase and the embedded aggregate, the volume concentration of aggregates and their interface characteristics. The stiffer the individual phases, the higher is the overall Young's modulus of concrete. Since aggregates are usually much stiffer than the cement paste, the Young's modulus of concrete increases with a higher volume ratio of aggregates. For further information on how these individual phases influence the overall properties, the reader is referred to [Alexander and Beushausen, 2009].

# Chapter 3

# Classical Continuum Mechanics

Any material is formed of a complex structure of molecules and is therefore not continuous. However, the classical theory of continuum mechanics describes the behaviour of material neglecting the structure of material on a smaller scale. Continuum mechanics studies the behaviour of an arbitrary continuous material body based on physical and material laws, i.e. to find its deformations, internal forces, stress, energy dissipation, etc.

This chapter provides a brief overview of the most important formulas and derivations of classical continuum mechanics needed within this research project. For further information about this topic, the reader is referred to [Mase and Mase, 1999].

## 3.1 Kinematics and Geometry

Consider an arbitrarily shaped continuous body defined in the three-dimensional manifold $\mathcal{B}$. Let $\mathcal{B} \subset \mathbb{E}(3)$, where $\mathbb{E}(3)$ is the Euclidian vector space. If the body is subjected to an external loading, it deforms and translates from its reference position to a current position $\mathcal{B}_t$ at a subsequent time $t \in \mathbb{R}$. This deformation of the body is represented by the mapping $\boldsymbol{\varphi}_t : \mathcal{B} \rightarrow \mathcal{B}_t$. The reference configuration $\mathcal{B}$ is defined as the undeformed body at a time $t_0$. The position of any material point can be described with a vector $\mathbf{X}$ in the reference configuration and with a vector $\mathbf{x}$ in the current configuration. The current position of a

particle at time $\mathbf{t}$ is given by

$$\mathbf{x} = \boldsymbol{\varphi}(\mathbf{X}, t)\,. \tag{3.1}$$

The displacement $\mathbf{u}$ is therefore simply defined by

$$\mathbf{u} = \mathbf{x} - \mathbf{X} \tag{3.2}$$

and the deformation gradient $\mathbf{F}$ by

$$\mathbf{F} = \frac{\partial \mathbf{x}}{\partial \mathbf{X}}, \tag{3.3}$$

where the Jacobian $J = \det \mathbf{F} > 0$. The Jacobian is a scalar denoting the change in volume of a infinitesimal region undergoing deformation, i.e. change in volume divided by original volume. This relation can be expressed as

$$dv = J\, dV\,, \tag{3.4}$$

where $dv$ and $dV$ are volume elements in the current and reference configuration respectively. The material is considered to be incompressible when $J = 1$. Similarily, a surface element in the reference configuration $dA$ with its unit normal vector $\mathbf{n}$ can be related to its counterpart in the current configuration $da$ with its unit normal $\boldsymbol{\nu}$

$$\boldsymbol{\nu}\, da = J\, \mathbf{F}^{-T}\, \mathbf{n}\, dA \tag{3.5}$$

and a line element by

$$d\mathbf{x} = \mathbf{F}\, d\mathbf{X}\,. \tag{3.6}$$

For later use, the material derivative of the Jacobian is given by

$$\dot{J} = J \operatorname{div} \dot{\mathbf{x}}\,, \tag{3.7}$$

where the operator div is the divergence with respect to the current configuration.

Since $\mathbf{x} = \mathbf{X} + \mathbf{u}$, the deformation gradient can also be defined by

$$\mathbf{F} = \frac{\partial \mathbf{X}}{\partial \mathbf{X}} + \frac{\partial \mathbf{u}}{\partial \mathbf{X}} = \mathbf{I} + \operatorname{Grad} \mathbf{u}, \tag{3.8}$$

where $\mathbf{I}$ is the identity tensor and Grad denotes the gradient operator with respect to the reference configuration. $\mathbf{F}$ therefore maps the deformation between the reference and the current configurations.

The right-hand *Cauchy-Green* deformation tensor $\mathbf{C}$ is a non-linear measure of strain and is defined as

$$\mathbf{C} = \mathbf{F}^T \mathbf{F}, \tag{3.9}$$

or alternatively, the *Green-Lagrange strain tensor* $\mathbf{E}$ defined as follows

$$\mathbf{E} = \frac{1}{2} (\mathbf{C} - \mathbf{1}) . \tag{3.10}$$

## 3.2 Stress Measures

Stress is a measure of force intensity in a body or on its bounding surface. There are two types of forces which can be distinguished from one each other. Body forces, denoted $\mathbf{b}$, act on volume elements and are distributed throughout the body. Gravity is an example of a body force and is described in either force per unit mass or force per unit volume. The other type of forces are surface forces or so-called tractions, denoted $\mathbf{t}$. Surface forces have dimensions of force per unit area.

The *Surface traction* $\mathbf{t}^{(\nu)}$ can be seen as the force acting on a cut surface of a body and is defined as

$$\lim_{\Delta a \to 0} \frac{\Delta \mathbf{f}}{\Delta a} = \frac{d\mathbf{f}}{da} = \mathbf{t}^{(\boldsymbol{\nu})} , \tag{3.11}$$

where $\Delta \mathbf{f}$ is the force acting on an area $\Delta a$ and $\mathbf{t}^{(\nu)}$ is acting on a surface with its unit normal vector $\boldsymbol{\nu}$.

The force vector can be written as linear transformation of its unit normal vector $\boldsymbol{\nu}$ as follows

$$\mathbf{t}^{(\boldsymbol{\nu})} = \boldsymbol{\sigma}^T \boldsymbol{\nu} \tag{3.12}$$

where $\boldsymbol{\sigma}$ is the *Cauchy stress tensor*. Equation 3.12 is referred as the *Cauchy stress principle* and it associates the stress vector $\mathbf{t}^{(\nu)}$ with each cutting plane and its normal vector $\boldsymbol{\nu}$ at a given point. Note, Equation 3.12 can also be written in the reference configuration as

$$\mathbf{t}^{(\boldsymbol{n})} = \boldsymbol{P}\boldsymbol{n} \tag{3.13}$$

where $\boldsymbol{P}$ is the *first Piola-Kirchhoff* stress tensor. $\mathbf{t}^{(\boldsymbol{n})}$ is defined similarly to Equation 3.11 but referring to a surface element $dA$ and its unit normal vector $\mathbf{n}$. Furthermore, the first Piola-Kirchhoff stress tensor can be linked with the *second Piola-Kirchhoff* tensor $\mathbf{S}$ by making use of the deformation gradient

$$\mathbf{P} = \mathbf{F}\mathbf{S}\,. \tag{3.14}$$

## 3.3 Balance Laws

Balance laws are fundamental expressions of the conservation of some physical quantity which are applicable to all material continua and result in equations that must always be satisfied. The balance laws needed in this research project are conservation of mass, linear momentum and angular momentum. For information about other balance laws, the reader is referred to [Mase and Mase, 1999].

### 3.3.1 Conservation of Mass

Every material volume element is endowed with a mass $m$. The mass density of a body can be determined by dividing the mass by the volume of a small body and taking its limit

$$\rho = \lim_{\Delta v \to 0} \frac{\Delta m}{\Delta v} \tag{3.15}$$

where $\Delta m$ is assumed to be absolutely continuous. The mass of a body in the current configuration is then given by the integral

$$m = \int_{\mathcal{B}_t} \rho\,(\mathbf{x}, t)\ \, dv\,. \tag{3.16}$$

In the same way, the mass of a body in the reference configuration is given by

$$m = \int_{\mathcal{B}} \rho_0\,(\mathbf{X})\ \, dV\,. \tag{3.17}$$

The law of *conservation of mass* asserts that the total mass of a body is conserved with motion. The material derivative of Eq. 3.16 is therefore zero

$$\dot{m} = \frac{d}{dt}\int_{\mathcal{B}_t} \rho\,(\mathbf{x}, t)\ \, dv = \int_{\mathcal{B}_t} \left\{\, \dot{\rho}\,(\mathbf{x}, t) + \rho\,(\mathbf{x}, t)\ J \operatorname{div} \dot{\mathbf{x}} \,\right\} dv = 0\,, \tag{3.18}$$

where the relations (Eq. 3.4) and (Eq. 3.7) were used. Since this equation is valid in any part of the continuum, the integrand of this equation must vanish, which results in the so called *continuity equation* in the Eulerian form

$$\dot{\rho}\,(\mathbf{x}, t) + \rho\,(\mathbf{x}, t)\ J \operatorname{div} \dot{\mathbf{x}} = 0\,. \tag{3.19}$$

The law of conservation of mass also requires the mass to be the same in all configurations. Therefore, if we equate Equation 3.16 and 3.17 we obtain

$$m = \int_{\mathcal{B}} \rho_0\,(\mathbf{X})\ \, dV = \int_{\mathcal{B}_t} \rho\,(\mathbf{x}, t)\ \, dv\,, \tag{3.20}$$

Noting that $\mathbf{x} = \mathbf{x}(\mathbf{X}, t)$, making use of Equation 3.4 and collecting terms, the following expression is obtained

$$\int_{\mathcal{B}} \left\{\, \rho\,(\mathbf{X}, t)\ J - \rho_0\,(\mathbf{X}) \,\right\} dV = 0\,. \tag{3.21}$$

This is again valid for any arbitrary volume element

$$\rho\left(\mathbf{X},t\right)\ J=\rho_0\left(\mathbf{X}\right), \tag{3.22}$$

which is called the Lagrangian, or material, form of the continuity equation. Also, the derivative of the mass density is zero

$$\frac{d}{dt}\left(\rho\left(\mathbf{X},t\right)\ J\right)=0. \tag{3.23}$$

### 3.3.2 Linear Momentum Principle

The linear momentum principle is based on Newton's second law of motion which states that a force acting on a body is equal to its mass times acceleration. Let a body be subjected to a body force $\mathbf{b}$ and its bounding surface $\partial\mathcal{B}$ be subjected to a surface traction $\mathbf{t}^{(\boldsymbol{\nu})}$. The principle of linear momentum states then that the time rate of change of the linear momentum is equal to the resultant force acting on the body

$$\frac{d}{dt}\int\limits_{\mathcal{B}_t}\rho\left(\mathbf{x},t\right)\ \dot{\mathbf{x}}\ dv=\int\limits_{\partial\mathcal{B}_t}\mathbf{t}^{(\boldsymbol{\nu})}\left(\mathbf{x},t\right)\ da+\int\limits_{\mathcal{B}_t}\mathbf{b}\left(\mathbf{x},t\right)\ dv\,. \tag{3.24}$$

Substituting Equation 3.12 for the surface traction and converting the surface integral to a volume integral by making use of *Gauss's divergence theorem*, the above equation can be written as

$$\int\limits_{\mathcal{B}_t}\left\{\ \rho\left(\mathbf{x},t\right)\ \ddot{\mathbf{x}}-\operatorname{div}\boldsymbol{\sigma}^T-\mathbf{b}\left(\mathbf{x},t\right)\ \right\}\ dv=\mathbf{0}\,. \tag{3.25}$$

Again, this equation is valid in any arbitrary material body so the integrand must vanish, resulting in

$$\rho\left(\mathbf{x},t\right)\ \ddot{\mathbf{x}}-\operatorname{div}\boldsymbol{\sigma}^T-\mathbf{b}\left(\mathbf{x},t\right)=0\,, \tag{3.26}$$

which is referred as the *local equation of motion*. If the velocity field is zero or constant so that $\ddot{\mathbf{x}}=0$, the equation of motion reduces to the *equilibrium equation*

$$\operatorname{div}\boldsymbol{\sigma}^T+\mathbf{b}\left(\mathbf{x},t\right)=\mathbf{0}\,. \tag{3.27}$$

Referring all quantities in Eq. (3.24) to the reference configuration, the *global equation of motion* in its material form is given by

$$\frac{d}{dt}\int_{\mathcal{B}} \rho_0\, \dot{\mathbf{x}}\,(\mathbf{X},t)\; dV = \int_{\partial\mathcal{B}} \mathbf{t}^{(\mathbf{n})}\,(\mathbf{X},t)\; dA + \int_{\mathcal{B}} \mathbf{b}\,(\mathbf{X},t)\; dV\,. \tag{3.28}$$

Following the same procedure, the *Lagrangian equation of motion* is obtained

$$\mathrm{Div}\,\mathbf{P} + \mathbf{b}\,(\mathbf{X},t) = \rho_0\, \ddot{\mathbf{x}}\,(\mathbf{X},t)\;. \tag{3.29}$$

If the acceleration field is zero, the *Lagrangian equilibrium equation* is given by

$$\mathrm{Div}\,\mathbf{P}\,(\mathbf{X},t) + \mathbf{b}\,(\mathbf{X},t) = \mathbf{0}\,. \tag{3.30}$$

### 3.3.3 Angular Momentum Principle

For the sake of completeness and to prove the symmetry of the of the Cauchy stress tensor, the angular momentum principle is outlined. The angular momentum is the moment of the linear momentum with respect to some reference point, usually the origin of a coordinate system. The time rate of change of the angular momentum of a body with respect to a reference point is equal to the resulting moment of the surface and body forces acting on the body $\mathcal{B}$ with respect to that point, as given by

$$\frac{d}{dt}\int_{\mathcal{B}_t} \mathbf{x}\times\rho\,(\mathbf{x},t)\;\dot{\mathbf{x}}\; dv = \int_{\partial\mathcal{B}_t} \mathbf{x}\times\mathbf{t}^{(\boldsymbol{\nu})}\,(\mathbf{x},t)\; da + \int_{\mathcal{B}_t} \mathbf{x}\times\mathbf{b}\,(\mathbf{x},t)\; dv\,. \tag{3.31}$$

Note that the operation $\mathbf{a}\times\mathbf{b}$ denotes the cross product of two vectors.

A similar procedure is used as for the linear momentum principle (Eq. 3.25) to obtain

$$\int_{\mathcal{B}_t} \Big\{\, \mathbf{x}\times\rho\,(\mathbf{x},t)\;\ddot{\mathbf{x}} - \mathrm{div}\,\left(\mathbf{x}\times\boldsymbol{\sigma}^T\right) - \mathbf{x}\times\mathbf{b}\,(\mathbf{x},t)\,\Big\}\; dv = \mathbf{0}\,, \tag{3.32}$$

where the divergence term with respect to the current configuration is evaluated as follows

$$\mathrm{div}\,\left(\mathbf{x}\times\boldsymbol{\sigma}^T\right) = \mathrm{grad}\,\mathbf{x}\times\boldsymbol{\sigma}^T + \mathbf{x}\times\mathrm{div}\,\boldsymbol{\sigma}^T\,. \tag{3.33}$$

The global principle of angular momentum in its spatial form is expressed by

$$\int_{\mathcal{B}_t} \Big\{ \mathbf{x} \times \rho\,(\mathbf{x},t)\ \ddot{\mathbf{x}} + \boldsymbol{\epsilon} : \boldsymbol{\sigma}^T - \mathbf{x} \times \operatorname{div} \boldsymbol{\sigma}^T - \mathbf{x} \times \mathbf{b}\,(\mathbf{x},t) \Big\}\ dv = \mathbf{0} \tag{3.34}$$

and the relation $\operatorname{grad} \mathbf{x} = \mathbf{1}$ holds. The corresponding field equation is expressed by

$$\mathbf{x} \times \rho\,(\mathbf{x},t)\ \ddot{\mathbf{x}} - \mathbf{x} \times \operatorname{div} \boldsymbol{\sigma}^T - \mathbf{x} \times \mathbf{b}\,(\mathbf{x},t) + \boldsymbol{\epsilon} : \boldsymbol{\sigma}^T = \mathbf{0}\,, \tag{3.35}$$

because $\mathcal{B}_t$ is arbitrary and the integrand in Equation 3.34 must vanish. Note, $\boldsymbol{\epsilon}$ is the basic skew-symmetric third order *Levi-Civita tensor*, also known as permutation tensor. Using Eq. (3.26) leads to

$$\boldsymbol{\epsilon} : \boldsymbol{\sigma}^T = \mathbf{0}\,. \tag{3.36}$$

This last equation demonstrates that $\sigma_{kj} = \sigma_{jk}$ holds true and therefore confirming the symmetry of the Cauchy stress tensor. Note; it is assumed in this derivation of the angular momentum principle that no body or surface couples act on the body. The classical continuum does not allow for complex interaction of continuum points [Murdoch, 2004]. Hence, neighbours of second order are unconsidered. If any body or surface couples do act, the material is said to be a polar material, and the symmetry property of $\boldsymbol{\sigma}$ no longer holds.

Referring all quantities in Eq. (3.31) to the reference configuration, the angular momentum principle in the Lagrangian configuration is given by

$$\begin{aligned} \frac{d}{dt} \int_{\mathcal{B}} \mathbf{x}\,(\mathbf{X},t) \times \rho_0\, \dot{\mathbf{x}}\,(\mathbf{X},t)\ dV \quad &= \\ \int_{\partial\mathcal{B}} \mathbf{x}\,(\mathbf{X},t) \times \mathbf{t}^{(\mathbf{n})}\,(\mathbf{X},t)\ dA \quad &+ \quad \int_{\mathcal{B}} \mathbf{x}\,(\mathbf{X},t) \times \mathbf{b}\,(\mathbf{X},t)\ dV\,. \end{aligned} \tag{3.37}$$

Following the same procedures, Equation 3.34 becomes

$$\begin{aligned} \int_{\mathcal{B}} \Big\{ \mathbf{x}\,(\mathbf{X},t) \times \big(\rho_0\, \ddot{\mathbf{x}}\,(\mathbf{X},t) - \operatorname{Div} \mathbf{P} - \mathbf{b}\,(\mathbf{X},t)\big) - \\ - \operatorname{Grad} \mathbf{x}\,(\mathbf{X},t) \times \mathbf{P} \Big\}\ dV = \mathbf{0}\,, \end{aligned} \tag{3.38}$$

in the reference configuration. Again, the integrand must vanish and, using Equation 3.29, leads to

$$\mathbf{F} \times \mathbf{P} = \boldsymbol{\epsilon} : \left(\mathbf{F}\mathbf{P}^T\right) = \mathbf{0}\,, \tag{3.39}$$

which results in the following symmetry condition

$$\mathbf{F}\mathbf{P}^T = \mathbf{P}\mathbf{F}^T\,. \tag{3.40}$$

Recall, $\mathbf{P} = \mathbf{F}\mathbf{S}$ which finally results in the symmetry of the *second Piola-Kirchhoff stress tensor*

$$\mathbf{S}^T = \mathbf{S}\,. \tag{3.41}$$

# Chapter 4

# Micromorphic Continuum Mechanics

In classical continuum mechanics it is assumed that the considered material is homogeneous and the structure of material on a smaller scale is neglected. This assumption holds if the specimen is larger than the RVE (Section 1.1.2). However, if the specimen is smaller than the RVE, the micro-structure influences the overall behaviour and thus has to be taken into account. This is done by adding non-local information to governing and constitutive equations which address the behaviour of the constituents as a whole and its interaction with neighbouring constituents.

This chapter outlines a micromorphic continuum theory with multiple micro-spaces. The approach is based on a framework introduced in [Sansour, 1998] and as extension of [Sansour et al., 2010], where the generalised continuum is constructed as consisting of a macro- and micro- continuum. In this work, however, the theory is extended to consider multiple micro-spaces which makes the formulation more general and accurate. Each material point is associated with several independent micro-directors which refer to an internal length scale. Hence, in micromorphic continuum formulations it is possible to model size scale effects which relate to non-local material behaviour. The number of micro-spaces and their dimension may be freely chosen depending on the accuracy of the description of a physical property, but must be finite. The constitutive law is defined at the microscopic level and the geometrical specification of each micro-continuum is the only material input beyond those needed in a classical description. Unless it is otherwise stated, the variables are the same as defined in

the previous chapter.

## 4.1 Generalised Deformation and Strain Measures

In this section a theory of generalised micromorphic deformations is developed based on the theoretical framework for generalised continuum developed in [Sansour, 1998], which makes use of the mathematical concept of a fibre bundle (see for example [Choquet-Bruhat et al., 1982]). In the simplest case, the generalised space is constructed as the Cartesian product of a macro space $\mathcal{B} \subset \mathbb{E}(3)$ and a micro-space $\mathcal{S}$ which is written as $\mathcal{G} := \mathcal{B} \times \mathcal{S}$ (Fig. 4.1). However, in the current approach multiple superimposed micro-spaces $\mathcal{S}^I$ are considered with $I = 1, ...$ or $m$, i.e. $\mathcal{S}$ represents the sum of all superimposed micro-spaces. This definition assumes an additive structure of $\mathcal{G}$ which implies that the integration over the macro- and the micro-continua can be performed separately. The macro-space $\mathcal{B}$ is parameterized by the curvilinear coordinates $\vartheta^i$, $i = 1, 2, 3$ and the micro-space $\mathcal{S}$ by the curvilinear coordinates $\zeta^\alpha$. Here, and in what follows, Greek indices take the values $1, ...$ or $n$. The dimension of each micro-space $\mathcal{S}^I$ denoted by $n$ is arbitrary, but finite. Furthermore, the dimension and topology of the micro-space is dependent on $\vartheta^i$. Similar to classical continuum mechanics, each material point $\tilde{\mathbf{X}} \in \mathcal{G}$ is related to its spatial placement $\tilde{\mathbf{x}} \in \mathcal{G}_t$ at time $t \in \mathbb{R}$ by the mapping $\tilde{\boldsymbol{\varphi}}(t) : \mathcal{G} \longrightarrow \mathcal{G}_t$. For convenience, but without loss of generality, $\mathcal{G}$ is identified with the undeformed reference configuration at a fixed time $t_0$ in what follows. The tangent space $\mathcal{TG}$ in the reference configuration is defined by the pair $(\tilde{\mathbf{G}}_i \times \mathbf{I}_\alpha)$ given by

$$\tilde{\mathbf{G}}_i = \frac{\partial \tilde{\mathbf{X}}}{\partial \vartheta^i} \qquad \text{and} \qquad \mathbf{I}_\alpha = \frac{\partial \tilde{\mathbf{X}}}{\partial \zeta^\alpha}\,, \tag{4.1}$$

where the corresponding dual contra-variant vectors are denoted by $\tilde{\mathbf{G}}^i$ and $\mathbf{I}^\alpha$, respectively.

As shown in Figure 4.1, the placement vector $\tilde{\mathbf{x}}$ of a material point $P\,(\tilde{\mathbf{X}} \in \mathcal{G})$ is assumed to be of an additive nature and is the sum of its position in the macro-continuum $\mathbf{x} \in \mathcal{B}_t$ and in the superimposed micro-continua $\mathcal{S}_t$ as follows

$$\tilde{\mathbf{x}} = \mathbf{x} + \boldsymbol{\xi}\,, \qquad \text{with } \boldsymbol{\xi} \in \mathcal{S}_t\,. \tag{4.2}$$

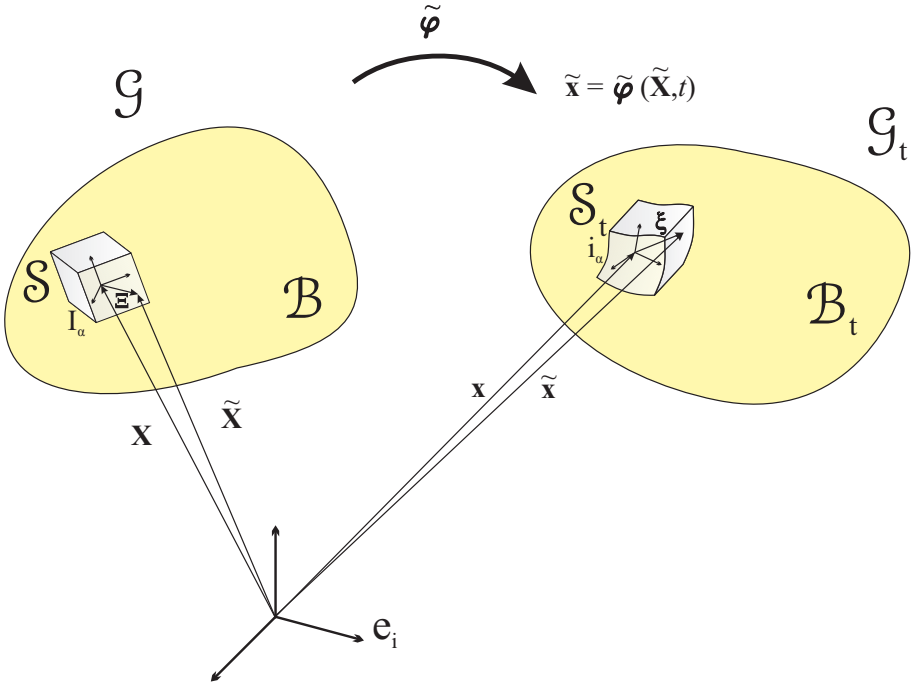


Figure 4.1: *Configuration Spaces*

Accordingly, in the reference configuration with $t = t_0$, the placement of a material point is given by

$$\tilde{\mathbf{X}} = \mathbf{X} + \boldsymbol{\Xi}\,, \qquad \text{with } \boldsymbol{\Xi} \in \mathcal{S}\,. \tag{4.3}$$

The placement vector $\tilde{\mathbf{x}}$ can also be written as [Sansour et al., 2010]

$$\tilde{\mathbf{x}} = \mathbf{x}\left(\vartheta^k, t\right) + \zeta^\alpha \left(1 + \zeta^\beta \chi_\beta\left(\vartheta^k, t\right)\right) \mathbf{a}_\alpha\left(\vartheta^k, t\right)\,. \tag{4.4}$$

The macro-placement vector $\mathbf{x}$ thus defines the origin of the micro-coordinate systems such that the micro-placement $\boldsymbol{\xi}$ is assumed to be relative to the macro-placement. With each micro-coordinate $\zeta^\alpha$ four extra degrees of freedom are associated which are the three components of $\mathbf{a}_\alpha$ and the scalar $\chi_\alpha$, respectively. The directors in current and reference confiugration are related via

$$\mathbf{a}_\alpha = \mathbf{a}^0_\alpha + \gamma_\alpha\,, \tag{4.5}$$

where $\gamma_\alpha$ denotes the increment or change of the director. $\mathbf{a}_\alpha^0$ are unit vectors and their directions can be freely chosen according to the specific topology of the micro-spaces as well as depending on the physical properties of the material due to its intrinsic structure.

The strain measures are defined in a similar manner to classical continuum mechanics. Taking the derivatives of $\tilde{\mathbf{x}}$ with respect to the macro-coordinates $\vartheta^i$

$$\begin{aligned}\tilde{\mathbf{x}}_{,i} &= \frac{\partial \tilde{\mathbf{x}}}{\partial \vartheta^i} = \mathbf{x}_{,i}\left(\vartheta^k,t\right) + \zeta^\alpha\,\zeta^\beta\,\chi_{\beta,i}\left(\vartheta^k,t\right)\,\mathbf{a}_\alpha\left(\vartheta^k,t\right) \\ &\quad + \zeta^\alpha\,\left(1+\zeta^\beta\,\chi_\beta\left(\vartheta^k,t\right)\right)\,\mathbf{a}_{\alpha,i}\left(\vartheta^k,t\right)\,, \end{aligned} \tag{4.6}$$

as well as with respect to the micro-coordinates $\zeta^\alpha$,

$$\tilde{\mathbf{x}}_{,\alpha} = \frac{\partial \tilde{\mathbf{x}}}{\partial \zeta^\alpha} = \mathbf{a}_\alpha\left(\vartheta^k,t\right) + \zeta^\beta\,\left(\chi_\beta\left(\vartheta^k,t\right)\,\mathbf{a}_\alpha\left(\vartheta^k,t\right)\; + \chi_\alpha\left(\vartheta^k,t\right)\,\mathbf{a}_\beta\left(\vartheta^k,t\right)\right)\,, \tag{4.7}$$

the generalized deformation gradient tensor can be expressed as follows

$$\begin{aligned}\tilde{\mathbf{F}} = &\Big[\mathbf{x}_{,i}\left(\vartheta^k,t\right) + \zeta^\alpha\,\zeta^\beta\,\chi_{\beta,i}\left(\vartheta^k,t\right)\,\mathbf{a}_\alpha\left(\vartheta^k,t\right) \\ &+\zeta^\alpha\,\left(1+\zeta^\beta\,\chi_\beta\left(\vartheta^k,t\right)\right)\,\mathbf{a}_{\alpha,i}\left(\vartheta^k,t\right)\Big]\otimes\tilde{\mathbf{G}}^i + \\ &\Big[\mathbf{a}_\alpha\left(\vartheta^k,t\right) + \zeta^\beta\,\left(\chi_\beta\left(\vartheta^k,t\right)\,\mathbf{a}_\alpha\left(\vartheta^k,t\right)\; + \chi_\alpha\left(\vartheta^k,t\right)\,\mathbf{a}_\beta\left(\vartheta^k,t\right)\right)\Big]\otimes\mathbf{I}^\alpha\,, \end{aligned} \tag{4.8}$$

where the operator $\otimes$ denotes the dyadic product of two vectors.

In order to formulate generalised strain measures based on Eq. (4.8), the generalised right *Cauchy-Green* deformation tensor is defined by

$$\begin{aligned}\tilde{\mathbf{C}} = \tilde{\mathbf{F}}^T\tilde{\mathbf{F}} = &\Big(\mathbf{x}_{,k}\cdot\mathbf{x}_{,l} + \zeta^\alpha\,\left(\mathbf{a}_{\alpha,k}\cdot\mathbf{x}_{,l} + \mathbf{x}_{,k}\cdot\mathbf{a}_{\alpha,l}\right)\Big)\;\tilde{\mathbf{G}}^k\otimes\tilde{\mathbf{G}}^l \\ &+\Big(\mathbf{x}_{,k}\cdot\mathbf{a}_\beta + \zeta^\alpha\,\mathbf{a}_{\alpha,k}\cdot\mathbf{a}_\beta + \zeta^\alpha\,\mathbf{x}_{,k}\cdot\left(\chi_\alpha\,\mathbf{a}_\beta + \chi_\beta\,\mathbf{a}_\alpha\right)\Big)\,\Big(\tilde{\mathbf{G}}^k\otimes\mathbf{I}^\beta + \mathbf{I}^\beta\otimes\tilde{\mathbf{G}}^k\Big) \\ &+\Big(\zeta^\alpha\,\left(\chi_\gamma\,\mathbf{a}_\alpha\cdot\mathbf{a}_\beta + \chi_\beta\,\mathbf{a}_\alpha\cdot\mathbf{a}_\gamma\right) + 2\,\zeta^\alpha\,\chi_\alpha\,\mathbf{a}_\beta\cdot\mathbf{a}_\gamma + \mathbf{a}_\beta\cdot\mathbf{a}_\gamma\Big)\;\mathbf{I}^\beta\otimes\mathbf{I}^\gamma \\ = &\;\mathbf{K}^0 + \zeta^\alpha\,\mathbf{K}^1_\alpha \quad \in \mathbb{E}^{3+n}\otimes\mathbb{E}^{3+n}, \end{aligned} \tag{4.9}$$

neglecting higher order terms in $\zeta^\alpha$ and considering only the dominant parts of $\tilde{\mathbf{C}}$ (constant and linear in $\zeta^\alpha$). Note, the operation $\mathbf{a}\cdot\mathbf{b}$ denotes the scalar product of two vectors. In

the present approach however, only two one-dimensional micro-spaces are considered, i.e. $m = 2$ and $n = 1$. Accordingly, the approach considers three classical displacements plus four non-classical degrees of freedom of each micro-space and $\tilde{\mathbf{C}} \in \mathbb{E}^4 \otimes \mathbb{E}^4$. The formulation can be described with a higher accuracy and generality, the higher the number of $m$ and $n$ is chosen. However, the calculation time is amplified with more general formulations due to the four extra degrees of freedom with each micro-space and micro-dimension. In the following the quasi-static case is assumed and no time dependency is considered.

The generalised *Lagrangian Green* strain tensor $\tilde{\mathbf{E}}$ is defined as

$$\tilde{\mathbf{E}} = \frac{1}{2}\left(\tilde{\mathbf{C}} - \tilde{\mathbf{I}}\right) , \tag{4.10}$$

where the identity tensor in this micromorphic approach can be defined as

$$\tilde{\mathbf{I}} = \tilde{\mathbf{G}}^k \otimes \tilde{\mathbf{G}}^k + \mathbf{a}^0_\gamma \otimes \mathbf{I}^\gamma + \mathbf{I}^\gamma \otimes \mathbf{a}^0_\gamma + \mathbf{I}^\gamma \otimes \mathbf{I}^\gamma . \tag{4.11}$$

## 4.2 Variational Principle for the Micromorphic Theory

The variational principle used in this approach can be defined in a similar manner as the variational principle based on the classical *right Cauchy-Green deformation tensor* $\mathbf{C}$. For this consider a non-linear boundary value problem in the domain $\mathcal{B} \times \mathcal{S}$ with the boundary $\partial\mathcal{B} \times \mathcal{S}$, where $\mathbf{n}$ defines the normal vector on $\partial\mathcal{B}$.

The variational principle for a deformable body in equilibrium states that the total external virtual work acting on the body is equal the internal virtual power. For the static case and considering only mechanical processes, the *first law of thermodynamics* provides the following variational statement

$$\delta\Psi - \mathcal{W}_{ext} = 0 , \tag{4.12}$$

where $\delta\Psi$ is the internal virtual power and $\mathcal{W}_{ext}$ is the external virtual work.

The external virtual work in the Lagrangian form is defined as follows

$$\mathcal{W}_{ext}\left(\mathbf{u}\right) = \int_{\mathcal{B}} \sum_{I=1}^{2} \Big[ \frac{n^I}{V_{\mathcal{S}^I}} \int_{\mathcal{S}^I} \tilde{\mathbf{b}}\left(\vartheta^k, \zeta^\beta\right) \cdot \delta\mathbf{u}\, dS \Big]\, dV + \int_{\partial\mathcal{B}} \sum_{I=1}^{2} \Big[ \frac{n^I}{V_{\mathcal{S}^I}} \int_{\mathcal{S}^I} \tilde{\mathbf{t}}^{(\mathbf{n})}\left(\eta^r, \zeta^\beta\right) \cdot \delta\mathbf{u}\, dS \Big]\, dA\,, \tag{4.13}$$

considering only micro-body forces $\tilde{\mathbf{b}}\left(\vartheta^k, \zeta^\beta\right)$ and $\tilde{\mathbf{t}}^{(\mathbf{n})}\left(\eta^r, \zeta^\beta\right)$, respectively. Note that $n^I$ is the Volume fraction of each micro-space and $\eta^r$, $r = 1, 2$ is the coordinate chart on $\partial\mathcal{B}$. Integrating the external virtual work over the micro-spaces $\mathcal{S}^I$ leads to

$$\mathcal{W}_{ext}\left(\mathbf{u}\right) = \int_{\mathcal{B}} \mathbf{b} \cdot \delta\mathbf{u}\; dV + \int_{\partial\mathcal{B}_N} \mathbf{t}^{(\mathbf{n})} \cdot \delta\mathbf{u}\; dA\,, \tag{4.14}$$

where the external body force $\mathbf{b}\left(\vartheta^k\right)$ is acting in $\mathcal{B}$, and the external traction $\mathbf{t}^{(\mathbf{n})}\left(\eta^r\right)$ is acting on the Neumann boundary $\partial\mathcal{B}_N$.

The internal virtual power in the Lagrangian form reads as follows

$$\delta\Psi = \frac{1}{2} \int_{\mathcal{B}} \sum_{I=1}^{2} \Big[ \frac{n^I}{V_{\mathcal{S}^I}} \int_{\mathcal{S}^I} \tilde{\mathbf{S}} : \delta\tilde{\mathbf{C}}\, dS \Big]\, dV\,, \tag{4.15}$$

where $\tilde{\mathbf{S}}^I$ is a generalised *second Piola-Kirchhoff*-like stress tensor. The relation holds $\mathbf{a} : \mathbf{b} = \operatorname{tr} \mathbf{a}\mathbf{b}^T$ for $\mathbf{a}, \mathbf{b}$ being second order tensors and tr denoting the trace operation. Note that the integration of Equations 4.13 and 4.15 over micro-continua $\mathcal{S}^I$ within the intervals $[-\frac{l^I}{2}, \frac{l^I}{2}]$ provides the incorporation of internal length scale parameters $l^I$ representing the assumed non-locality of the various material constituents.

Integrating the internal virtual power (Eq. 4.15) over the micro-spaces leads to $\mathcal{S}^I$

$$\delta\Psi = \int_{\mathcal{B}} \sum_{I=1}^{2} \Big\{ \mathbf{S}^I : \delta\mathbf{K}^0 + \mathbf{M}^I : \delta\mathbf{K}^1 \Big\}\; dV\,, \tag{4.16}$$

with the force stress

$$\mathbf{S}^I\left(\vartheta^k\right) = \frac{n^I}{V_{\mathcal{S}^I}} \int_{\mathcal{S}^I} \tilde{\mathbf{S}}\; dS \tag{4.17}$$

and higher-order and size-scale relevant stress

$$\mathbf{M}^I\left(\vartheta^k\right) = \frac{n^I}{V_{\mathcal{S}^I}} \int_{\mathcal{S}^I} \zeta\, \tilde{\mathbf{S}}\, dS\,. \tag{4.18}$$

and $\delta\tilde{\mathbf{C}} = \delta\mathbf{K}^0 + \zeta\,\delta\mathbf{K}^1$, refer to Equation 4.9. Note that the variational forms $\delta\mathbf{K}^0$ and $\delta\mathbf{K}^1$ are constant over $\mathcal{S}$. It can be seen that the integration over the micro-continuum $\mathcal{S}$ leads to two different stress measures. The tensor $\mathbf{S}$ is energy conjugate to a first-order tensor $\mathbf{K}^0$, i.e. multiplied with each other results into energy. The tensors $\mathbf{M}^I$ are energy conjugate to a second-order strain measure $\mathbf{K}^1$. Hence, only the tensors $\mathbf{M}^I$ contain the internal length scale and therefore contribute to the non-local size scale effects.

The variational principle is supplemented by essential boundary conditions, the so-called Dirichlet boundary conditions

$$\mathbf{u} = \mathbf{h}_u, \quad \mathbf{a} = \mathbf{h}, \quad \chi = h_\chi \quad \text{on } \partial\mathcal{B}_D\,, \tag{4.19}$$

where $\mathbf{h}_u$ and $\mathbf{h}$ are prescribed values for displacement and micro-displacement at the Dirichlet boundary. The boundary $\partial\mathcal{B}$ on the domain $\mathcal{B}$ consists of of the Dirichlet boundary $\partial\mathcal{B}_D = \partial\mathcal{B} \setminus \partial\mathcal{B}_N$.

## 4.3 Generalised Constitutive Law

It is assumed that the material behaviour is within the linear elastic regime in this research project. The classical *St. Venant-Kirchhoff* model was therefore chosen for the constitutive law. However, it is applied to extended tensor space in order to accommodate the generalised *Cauchy-Green* deformation tensor $\tilde{\mathbf{C}} \in \mathbb{E}^4 \otimes \mathbb{E}^4$. The St. Venant-Kirchhoff model is generally inappropriate in compression where large deformations occur. This is, however, not an issue in the current approach, as deformations of concrete are very small. The strain-energy density function is defined in terms of the *Lagrangian Green* strain tensor $\tilde{\mathbf{E}}$ as

$$\psi\left(\tilde{\mathbf{E}}\right) = \frac{\lambda^*}{2}\delta_{ij}\delta_{kl}\tilde{E}_{ij}\tilde{E}_{kl} + \mu^*\,\delta_{il}\delta_{jk}\tilde{E}_{ij}\tilde{E}_{kl}\,. \tag{4.20}$$

Note that we need to consider elastic material constants equivalent to the *Lamé constants* $\lambda$ and $\mu$, Young's modulus $E$ and Poissons ratio $\nu$ as used in a classical approach [Mase and Mase, 1999]. The material constants used in this approach are denoted by $\lambda^*$, $\mu^*$, $E^*$ and $\nu^*$ and defined as

$$\lambda^* = \frac{E^*\,\nu^*}{(1+\nu^*)\,(1-2\nu^*)} \qquad \text{and} \qquad \mu^* = \frac{E^*}{2\,(1+\nu^*)}\,. \tag{4.21}$$

Generally, Young's moduli used in a micromorphic approach are lower than the classical Young's moduli used in Hooke's law. This is clear, as the additional strain components in Equation 4.9 referring to the extended tensor space significantly influence the internal power (Eq. 4.15), i.e. adding extra components to it. Furthermore, $\lambda^*$ and $\mu^*$ are used to relate the normal and shear strain components with the stress, while $c_1$ and $c_2$ are referred to the higher-order terms in the constitutive tensor.

The *second Piola-Kirchhoff* stress tensor can then be calculated by taking the partial derivative of the strain energy function with respect to the strain tensor

$$\begin{aligned}
\tilde{S}_{ij} &= 2\frac{\partial \psi}{\partial \tilde{E}_{ij}} = \lambda^* \tilde{E}_{kk}\delta_{ij} + 2\mu^*\,\tilde{E}_{ij} \\
\tilde{S}_{i4} &= 2\frac{\partial \psi}{\partial \tilde{E}_{i4}} = c_1 \tilde{E}_{kk}\delta_{i4} + 2c_2\,\tilde{E}_{i4} \\
\tilde{S}_{44} &= 2\frac{\partial \psi}{\partial \tilde{E}_{44}} = c_1 \tilde{E}_{44} + 2c_2\,\tilde{E}_{44}\,,
\end{aligned} \tag{4.22}$$

where $i, j, k, l = 1, 3$ for a three-dimensional macro-space.

Finally, the non-zero entries of the fourth-order micro-constitutive tensor are derived by taking the partial derivative of the *second Piola-Kirchhoff* stress with respect to $\tilde{\mathbf{E}}$

$$\begin{aligned}
\tilde{\mathcal{C}}_{ijkl} &= \frac{\partial \tilde{S}_{ij}}{\partial \tilde{E}_{kl}} = \lambda^*\delta_{ij}\delta_{kl} + \mu^*\,(\delta_{ik}\delta_{jl} + \delta_{il}\delta_{jk}) \\
\tilde{\mathcal{C}}_{i4k4} &= \frac{\partial \tilde{S}_{i4}}{\partial \tilde{E}_{k4}} = c_2\delta_{ik} \\
\tilde{\mathcal{C}}_{4444} &= \frac{\partial \tilde{S}_{44}}{\partial \tilde{E}_{44}} = c_1 + 2c_2 \\
\tilde{\mathcal{C}}_{ij44} &= \frac{\partial \tilde{S}_{ij}}{\partial \tilde{E}_{44}} = c_1\delta_{ij}\,.
\end{aligned} \tag{4.23}$$

Equation 4.23 shows the classical entries of the micro-constitutive tensor in a region where $i, j, k, l = 1 - 3$ as well as the non-classical parts of the micro-constitutive tensor, denoted with a subscript 4. Again, since the total value of the micro-constitutive tensor must be equal to the one in the classical approach, the entries in the micromorphic approach subsequently have to be reduced. Note that the micro-constitutive tensor satisfies the symmetries

$$\tilde{\mathcal{C}}_{ijkl} = \tilde{\mathcal{C}}_{jikl} = \tilde{\mathcal{C}}_{ijlk} = \tilde{\mathcal{C}}_{klij} \,. \tag{4.24}$$

# Chapter 5

# Meshfree Modelling

For modelling purposes of the outlined micromorphic theory, a numerical method is implemented. A *Moving Least Squares* (MLS) based meshfree method proved to be more suitable than FEM since it is more flexible in designing approximation functions which provide any desired continuity [Skatulla, 2006]. Furthermore, the MLS based meshfree method is able to model problems which also involve higher order derivatives of the solution function. This chapter provides insight into some of the most important modelling related aspects of the current research project. Unless it is otherwise stated, the variables defined in the previous two chapters will be the reused in the current chapter. Further information about the meshfree method used in this research project can be found in [Dolbow and Belytschko, 1998]. A general overview of meshfree methods is presented in [Belytschko et al., 1996].

## 5.1 Moving Least Squares Method

Moving Least Squares is a method of smoothing and interpolating unstructured surface data, resulting in a surface which has a predefined continuity. The idea of moving least squares is to take any arbitrary fixed point $P \in \Omega$ and move it throughout the domain $\Omega$, where a weighted least squares fit is computed and evaluated for each point individually. Consider a globally defined function $u(\mathbf{x})$ over the field $\Omega \in \mathbb{R}^3$. The function $u(\mathbf{x})$ can be approximated

as

$$u^h(\mathbf{x}) = \mathbf{P}(\mathbf{x}) \cdot \mathbf{a}(\mathbf{x}) \,, \tag{5.1}$$

where $\mathbf{P}(\mathbf{x})$ is a polynomial basis vector of order $p$

$$\mathbf{P}(\mathbf{x}) = \left[1 \; x \; x^2, ...x^p\right] \,, \tag{5.2}$$

and $\mathbf{a}(\mathbf{x})$ is the vector of unknown coefficients

$$\mathbf{a}(\mathbf{x}) = \left[a_0(\mathbf{x}) \;\; a_1(\mathbf{x}) \;\; a_2(\mathbf{x}), ...a_p(\mathbf{x})\right] \,. \tag{5.3}$$

A weight function denoted by $\Phi_I$ is attached to each particle $P_I$ with its coordinates $\mathbf{x}_I$. The subscript $I$ denotes the particle number of the particles distributed over the domain $\Omega$. In a least squares' sense, a weighted error functional can be constructed as

$$J(\mathbf{a}(\mathbf{x})) = \sum_{I \in \Lambda} \Phi\left(\frac{\mathbf{x} - \mathbf{x}_I}{\varrho_I}\right) \left[u^h(\mathbf{x}) - u(\mathbf{x}_I)\right]^2 \,, \tag{5.4}$$

where $\varrho_I$ is the so-called *influence radius* which is defined as the size of the support. Note that the set $\Lambda$ is the sum of all particles that support the point $\mathbf{x}$, see Figure 5.1.

The unknown coefficients $\mathbf{a}(\mathbf{x})$ can be obtained by taking the partial derivatives of the weighted error functional (Equation 5.4) and solving for the coefficient vector $\mathbf{a}(\mathbf{x})$

$$\mathbf{a}(\mathbf{x}) = \left[\sum_{I=\Lambda} \mathbf{P}(\mathbf{x}_I)\, \mathbf{P}(\mathbf{x}_I)\, \Phi\left(\frac{\mathbf{x} - \mathbf{x}_I}{\varrho_I}\right)\right]^{-1} \sum_{I \in \Lambda} \mathbf{P}(\mathbf{x}_I) \; \Phi\left(\frac{\mathbf{x} - \mathbf{x}_I}{\varrho_I}\right) \; u_I \,. \tag{5.5}$$

Introducing the so-called *moment matrix* of the weight function $\Phi$

$$\mathbf{M}(\mathbf{x}) = \sum_{I=\Lambda} \mathbf{P}(\mathbf{x}_I)\, \mathbf{P}(\mathbf{x}_I)\, \Phi\left(\frac{\mathbf{x} - \mathbf{x}_I}{\varrho_I}\right) \,, \tag{5.6}$$

and expressing the MLS-approximation function for a particle $P_I$ as follows

$$N_I(\mathbf{x}) = \mathbf{P}(\mathbf{x}) \cdot \mathbf{M}^{-1}(\mathbf{x})\, \mathbf{P}(\mathbf{x}_I) \; \Phi\left(\frac{\mathbf{x} - \mathbf{x}_I}{\varrho_I}\right) \,, \tag{5.7}$$

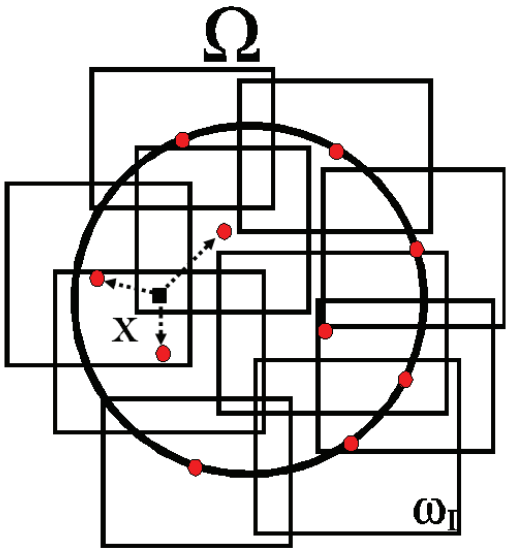


Figure 5.1: *Domain Covering*

Equation 5.1 takes then the form

$$u^h(\mathbf{x}) = \sum_{I \in \Lambda} N_I(\mathbf{x})\, u_I\,. \tag{5.8}$$

With increasing particle density, the influence radius of a particle can consequently be reduced. The smaller the influence radius, i.e. the value of $\varrho_I$, chosen, the more accurate the approximation $u^h(\mathbf{x})$ is.

## 5.2 Weight Function and Basis Polynomial

The support of each particle $P_I$ within a domain $\Omega$ is restricted

$$\Phi\left(\frac{\mathbf{x}-\mathbf{x}_I}{\varrho_I}\right) = \begin{cases} > 0 \quad , \quad \mathbf{x} \in supp\{\Phi\} \\ 0 \quad , \quad \mathbf{x} \notin supp\{\Phi\} \end{cases}, \tag{5.9}$$

where $\varrho_I$ denotes the influence radius of each particle. In other words, each particle has attached its own support $\omega_I$ which is also the same for the weight function $\varrho_I$. The influence zone of particles within a domain and, therefore also their corresponding shape functions

are overlapping, i.e. each point is supported by several particles as shown in Figure 5.1. The supports $\omega_I$ can be of any arbitrary shape but are usually discs or rectangles in two dimensions and balls or cuboids in three dimensions.

A weight function in three dimensions can be computed as follows [Dolbow and Belytschko, 1998]

$$\Phi\left(\frac{\mathbf{x}-\mathbf{x}_I}{\varrho}\right) \equiv w\left(\frac{x-x_I}{\varrho_x}\right) w\left(\frac{y-y_I}{\varrho_y}\right) w\left(\frac{z-z_I}{\varrho_z}\right) , \tag{5.10}$$

where the cuboid support is defined as

$$\omega_I := \left\{ \mathbf{x} \in \mathbb{R}^3 \,\middle|\, |x-x_I| \leq \varrho_x \wedge |y-y_I| \leq \varrho_y \wedge |z-z_I| \leq \varrho_z \right\} . \tag{5.11}$$

The choice of the shape function influences the resulting approximation of $u^h(\mathbf{x})$. In the implementation of the coding of this research project however, a cubic spline weight function is used

$$w(r) = \begin{cases} \frac{2}{3} - 4r^2 + 4r^3 & \text{for } |r| \leq \frac{1}{2} , \\ \frac{4}{3} - 4r + 4r^2 - \frac{4}{3}r^3 & \text{for } \frac{1}{2} < |r| \leq 1 , \\ 0 & \text{for } |r| > 1 , \end{cases} \tag{5.12}$$

where the normalised radius $r = (x - x_I)/\varrho$. This weight function possesses $C^2$ -continuity, i.e. first and second derivatives are equal. Figures 5.2 and 5.3 show the two-dimensional weight function and its first derivatives. This shape function proved to be most convenient with respect to accuracy and calculation time [Skatulla, 2006]. In contrary to FEM shape functions, the shape functions in MLS-based formulation do not fulfill the *Kronecker Delta* condition

$$N_I(\mathbf{x}_J) \neq \delta_{IJ}, \tag{5.13}$$

which states that the value of the shape function is equal to one at the specific particle $\mathbf{x}_J$ and equal to zero on all the other particles in the domain. As already mentioned beforehand,

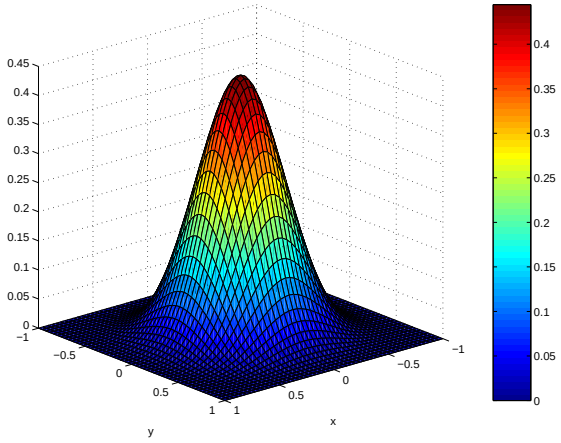


Figure 5.2: *Cubic Spline* $\Phi = w(x)\, w(y)$

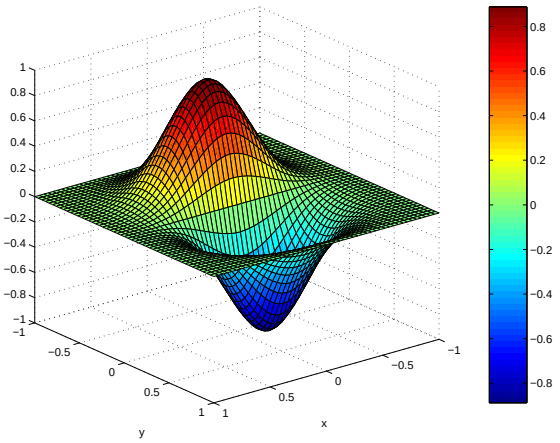


Figure 5.3: *First Order Derivative of the Cubic Spline* $\Phi_{,y} = \frac{1}{\varrho}\, w\, w_{,y}(y)$

each point is supported by several surrounding particles in this outlined MLS-based approach. Furthermore, the MLS algorithm requires a complete polynomial basis vector $\mathbf{P}(\mathbf{x})$ of order $p$. On the one hand, a high approximation accuracy can be achieved by chosing a high order polynomial. On the other hand, a higher-order polynomial requires larger particle support which leads to a large bandwith of the stiffness matrix and hence, higher computing time. A first order polynomial would be sufficient for the current research study, as the variational formulation contains only first order derivatives of the solution function $\mathbf{u}(\mathbf{x})$ and the vector of unknown coefficients $\mathbf{a}(\mathbf{x})$. In this study however, a Pascal polynomial of second order is used, which implies $p = 2$. A second order polynomial was found to be optimal with respect to accuracy and computation time [Skatulla, 2006]. The elements of a polynomial basis of the Pascal type are defined by

$$(x + y + z)^p \ , \tag{5.14}$$

which are given by the so-called *Binomian* formulae. The number of elements of vector $\mathbf{P}(\mathbf{x})$ is given as $l = \frac{1}{6}(p+1)(p+2)(p+3)$, i.e. the implemented quadratic basis vector contains 10 elements.

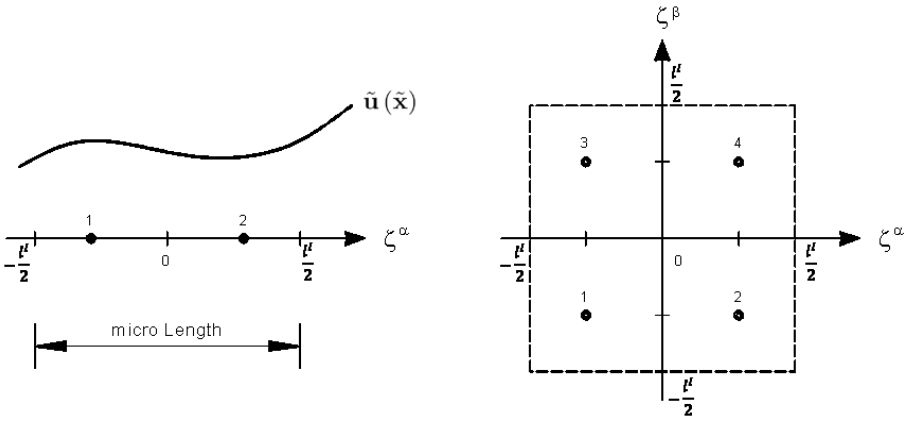


Figure 5.4: *Micro-Integration Grid in One and Two Dimensions*

## 5.3 Numerical Integration

In the presented micromorphic continuum theory, two micro-spaces $\mathcal{S}$ are associated with each macro material point $\mathbf{X} \in \mathcal{B}$. It is assumed that each micro-space possesses the same geometry throughout the macro continuum. The integration over the micro-spaces is performed separately using second order *Gauss quadrature*. The order of this integration method was chosen in accordance to the order of the basis polynomial used for the MLS-approximation scheme. For the micro-integration, a background mesh is laid over the integration cell, where its element size was chosen to be equal to the micro-coordinates $\zeta^\alpha$. Hence, each micro-space is one numerical integration grid. The dimension of $\mathcal{S}^I$ was chosen to be one, which is represented by a single straight line element. The coordinates and weights of the micro-integration points within each micro-space $\mathcal{S}^I$ are approximated by means of FEM shape functions. Figure 5.4 shows a one-dimensional and two-dimensional micro-space with its corresponding integration points of a second-order quadrature.

## 5.4 Enforcement of Boundary Conditions

By dealing with boundary conditions in MLS-based meshfree methods, the enforcement of essential boundary conditions is a critical issue. Considering a boundary value problem on

a domain $\Omega \in \mathbb{R}^3$ with boundary $\partial\Omega$

$$\mathcal{L}\mathbf{u}(\mathbf{x}) = \mathbf{f}(\mathbf{x}), \qquad \mathbf{x} \in \Omega \tag{5.15}$$

$$\mathbf{u}(\mathbf{x}) = \hat{\mathbf{u}}(\mathbf{x}), \qquad \mathbf{x} \in \partial\Omega_D, \tag{5.16}$$

where $\mathcal{L}$ is a linear operator and $\partial\Omega_D$ denotes the Dirichlet boundary. Multiplication with a weight function $\mathbf{w}(\mathbf{x})$ and integrating by parts leads from the strong form (Equation 5.15) to the weak form of the problem

$$a(\mathbf{w}(\mathbf{x}), \mathbf{u}(\mathbf{x}))_{L_2(\Omega)} = (\mathbf{w}(\mathbf{x}), \mathbf{f}(\mathbf{x}))_{L_2(\Omega)}, \tag{5.17}$$

where $\mathbf{w}(\mathbf{x})$ is arbitrary in $\Omega$ and assumed to be zero on $\partial\Omega_D$.

The solution function $\mathbf{u}(\mathbf{x})$ and the weight function $\mathbf{w}(\mathbf{x})$ are discretised using shape functions $\mathbf{N}_I(\mathbf{x})$

$$\mathbf{u}^h(\mathbf{x}) = \sum_{I \in \Lambda} \mathbf{N}_I(\mathbf{x})\,\mathbf{d}_I = \mathbf{N}(\mathbf{x})\,\mathbf{d} \tag{5.18}$$

$$\mathbf{w}^h(\mathbf{x}) = \sum_{I \in \Lambda} \mathbf{N}_I(\mathbf{x})\,\mathbf{c}_I = \mathbf{N}(\mathbf{x})\,\mathbf{c}, \tag{5.19}$$

where $\mathbf{d}_I$ and $\mathbf{c}_I$ are the trial and test function degrees of freedom. Finally, the matrix form of the discretised equation is

$$\mathbf{c} \cdot \mathbf{r} = 0 \quad \text{(weighted residual vector)}, \tag{5.20}$$

$$\mathbf{r} = \mathbf{K}\mathbf{d} - \mathbf{f} \quad \text{(residual vector)}, \tag{5.21}$$

$$\mathbf{K} = a(\mathbf{N}(\mathbf{x}), \mathbf{N}(\mathbf{x})) \quad \text{(stiffness matrix)}, \tag{5.22}$$

$$\mathbf{f} = (\mathbf{N}(x), \mathbf{f}(\mathbf{x})) \quad \text{(force vector)}. \tag{5.23}$$

### 5.4.1 Corrected Collocation Method

As mentioned earlier, the MLS approximation functions for a particle $P_I$ (Equation 5.7) do not satisfy the *Kronecker Delta* condition. Hence, the particle parameters $u_I$ are not equal to the value of the approximation function $\mathbf{u}^h(\mathbf{x})$ at particle $P_I$. The traditional boundary collocation method, which is used in the FE method, can therefore not be used in MLS-based meshfree methods. Wagner and Liu [2000] presented a solution to this problem by introducing the *corrected collocation method*. In the following, the corrected collocation method, applied to the linear boundary value problem, is outlined. A comparison between the traditional and modified method as well as numerical tests of this method can be found in [Wagner and Liu, 2000].

As it is done in the traditional method, the total number of particles $n$ can be divided into the number of Dirichlet boundary particles $n_b \in \partial\Omega_D$ and the number of Neumann boundary particles combined with those being placed on the interior domain $n_{nb} \in \tilde{\Omega} = \Omega \setminus \partial\Omega_D$

$$n = n_b + n_{nb}\,. \tag{5.24}$$

Hence, the partition can be written as

$$\mathbf{d} = \begin{Bmatrix} \mathbf{d}_b \\ \\ \mathbf{d}_{nb} \end{Bmatrix}, \qquad \mathbf{c} = \begin{Bmatrix} \mathbf{c}_b \\ \\ \mathbf{c}_{nb} \end{Bmatrix}, \qquad \mathbf{r} = \begin{Bmatrix} \mathbf{r}_b \\ \\ \mathbf{r}_{nb} \end{Bmatrix}. \tag{5.25}$$

The weight function (Equation 5.19) is partitioned similarly

$$\left\{w^h(x_I)\right\} = \begin{Bmatrix} \mathbf{w}_b^h \\ \\ \mathbf{w}_{nb}^h \end{Bmatrix} = \begin{bmatrix} \mathbf{A} & \mathbf{B} \\ \\ \mathbf{C} & \mathbf{D} \end{bmatrix} \begin{Bmatrix} \mathbf{c}_b \\ \\ \mathbf{c}_{nb} \end{Bmatrix}, \quad I \in \Lambda\,. \tag{5.26}$$

A new test function is defined by replacing $\mathbf{w}_{nb}^h$ by the particle degrees of freedom $\mathbf{c}_{nb}$

$$\tilde{\mathbf{c}} = \begin{Bmatrix} \mathbf{w}_b \\ \\ \mathbf{c}_{nb} \end{Bmatrix} = \begin{bmatrix} \mathbf{A} & \mathbf{B} \\ \\ \mathbf{0} & \mathbf{I} \end{bmatrix} \begin{Bmatrix} \mathbf{c}_b \\ \\ \mathbf{c}_{nb} \end{Bmatrix} = \tilde{\mathbf{N}}\mathbf{c}\,, \tag{5.27}$$

where $\mathbf{I}$ is the $n_{nb} \times n_{nb}$ identity matrix. The solution function $u^h(\mathbf{x})$ is defined in the same way

$$\tilde{\mathbf{d}} = \left\{ \begin{array}{c} \mathbf{u}_b \\ \mathbf{d}_{nb} \end{array} \right\} = \left\{ \begin{array}{cc} \mathbf{A} & \mathbf{B} \\ \mathbf{0} & \mathbf{1} \end{array} \right\} \left\{ \begin{array}{c} \mathbf{d}_b \\ \mathbf{d}_{nb} \end{array} \right\} = \tilde{\mathbf{N}}\mathbf{d}\,. \tag{5.28}$$

Note, the inverse of $\tilde{\mathbf{N}}$ as well as its transpose is expressed as

$$\tilde{\mathbf{N}}^{-1} = \left\{ \begin{array}{cc} \mathbf{A}^{-1} & \mathbf{A}^{-1}\mathbf{B} \\ \mathbf{0} & \mathbf{1} \end{array} \right\}, \qquad \left(\tilde{\mathbf{N}}^{-1}\right)^T = \left\{ \begin{array}{cc} \left(\mathbf{A}^{-1}\right)^T & \mathbf{0} \\ -\mathbf{B}^T\left(\mathbf{A}^{-1}\right)^T & \mathbf{1} \end{array} \right\}. \tag{5.29}$$

The weak form (Equation 5.20 and 5.21) can be written in terms of $\tilde{\mathbf{c}}$ and $\tilde{\mathbf{d}}$

$$\tilde{\mathbf{c}}^T\left(\tilde{\mathbf{K}}\tilde{\mathbf{d}} - \tilde{\mathbf{f}}\right) = 0\,, \tag{5.30}$$

where

$$\tilde{\mathbf{K}} = \left(\tilde{\mathbf{N}}^{-1}\right)^T \mathbf{K}\tilde{\mathbf{N}}^{-1} \tag{5.31}$$

$$\tilde{\mathbf{f}} = \left(\tilde{\mathbf{N}}^{-1}\right)^T \mathbf{f}\,. \tag{5.32}$$

Finally, partitioning $\tilde{\mathbf{c}}$ and $\tilde{\mathbf{d}}$ results into

$$\left[\tilde{\mathbf{c}}_b^T \;\; \tilde{\mathbf{c}}_{nb}^T\right] \left( \tilde{\mathbf{K}} \left\{ \begin{array}{c} \tilde{\mathbf{d}}_b^T \\ \tilde{\mathbf{d}}_{nb}^T \end{array} \right\} - \tilde{\mathbf{f}} \right) = 0\,. \tag{5.33}$$

Note that $\tilde{\mathbf{c}}_b$ is set to zero because it is assumed that the weight function $w^h(\mathbf{x})$ vanishes on $\partial\Omega_D$.

# Chapter 6

# Example 1

In this section the first example is presented to demonstrate the applicability of the theory. The Young's moduli of different concrete cylinders are calculated according to the outlined micromorphic theory in Chapter 4. The specimen size (see Figure 6.1) as well as the volume ratio between aggregates and mortar matrix is kept constant for all specimens while the aggregate size ranges from 6.7 mm to 26.5 mm. Based on the change of internal length scale parameter, i.e. changing coarse aggregate size, size scale effects are expected to be seen in this example. The objectives of this example are to test the micromorphic formulation and its behaviour with regard to additional material parameters. Size scale effects on a concrete specimen under uniaxial compression will be qualitatively modelled. Furthermore it is outlined how the model can be calibrated.

## 6.1 Simulations

The material is considered as a two-phase composite consisting of coarse aggregates embedded in a mortar matrix. Table 6.1 displays the chosen material properties used in the model. It is assumed that the material behaviour is within the linear elastic regime, which holds true if the compressive load does not exceed one-third of the failure load. The classical *St. Venant-Kirchhoff* model was therefore chosen, however it is applied to extended tensor space

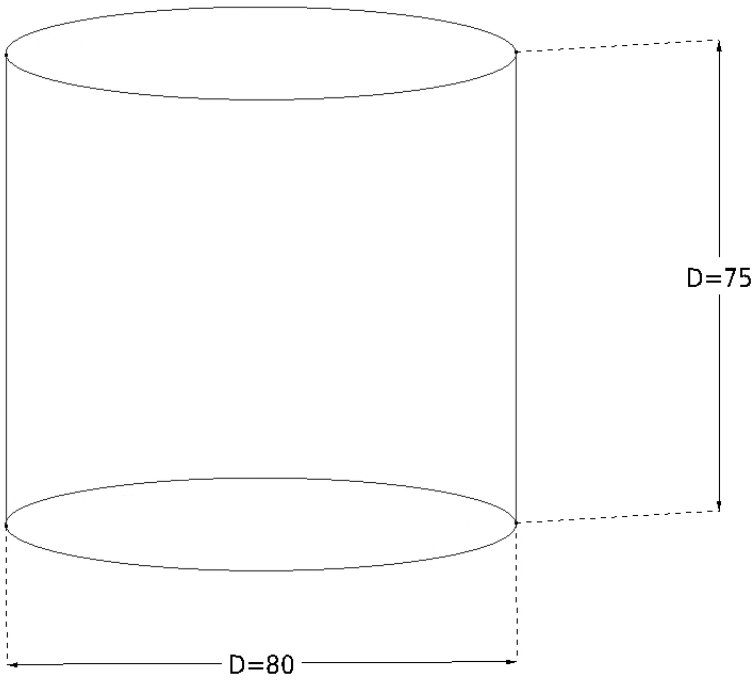


Figure 6.1: *Specimen Dimension*

in order to accommodate the generalised *Cauchy-Green* deformation tensor $\tilde{\mathbf{C}} \in \mathbb{E}^4 \otimes \mathbb{E}^4$. Due

Table 6.1: *Constitutive Parameters*

| | Unit | Aggregates | Matrix |
|---|---|---|---|
| $E^*$ | [GPa] | varies | 15 |
| $\nu^*$ | [-] | 0.2 | 0.2 |
| $c_1$ | [GPa] | varies | 8.33 |
| $c_2$ | [GPa] | varies | 12.5 |
| $l^I$ | [mm] | varies | 1 |
| $n$ | [%] | 40 | 60 |

to uniaxial compression of the specimen, the largest stress components that the material will experience are normal forces with a normal parallel to the applied load. The micro-directors in the undeformed configuration are therefore chosen to be parallel to the applied load, i.e.

$$\mathbf{a}_\alpha^0 = \mathbf{e}_3. \tag{6.1}$$

The internal length scale was set to 1 for the matrix and computed as follows

$$l_{agg} = \alpha d \tag{6.2}$$

for the aggregate, where $d$ refers to the different aggregate sizes. Equation 6.2 converts the three-dimensional shape of the aggregate to the one-dimensional micro-length. In this research project, the parameter $\alpha$ takes into account, in a very simplified fashion, the variation of geometry, position and surface structure of the aggregates. Note that the materials micro-structure is homogenised in a mathematical fashion, rather than by exactly modelling the micro-structural features. The value of parameter $\alpha$ corresponding to different aggregate shapes needs to be investigated in experiments. It will be shown later that a change in $\alpha$ leads to a change in magnitude of the size scale effects.

The overall Young's modulus of the concrete mix is computed by simple volume averaging

$$E_{concrete} = n_I \cdot E_{agg}^{eff*} + n_{II} \cdot E_{matrix}^{*} \,, \tag{6.3}$$

where the volume fractions of the two phases and their corresponding micro-spaces are denoted by $n$. To achieve meaningful results however, the actual aggregate stiffness needs to be reduced to an effective stiffness $E_{agg}^{eff*}$ of the aggregates as explained in Section 6.3.1. The Young's modulus of the matrix was chosen to be 15 GPa whereas the effective Young's modulus of the aggregates is used as a second calibration factor for the model. It should be noted that at this first example of the outlined model, the emphasis lies on qualitatively modelling trends, not in the modelling of true concrete properties.

The calculations were performed in a displacement control mode. The displacements on the bottom plane of the cylindrical specimen are fixed in all three axes. On the top plane only the tangential displacements components are fixed and the component parallel to the cylinder axis was set to 1 mm. The resulting internal traction component normal to the top plane is then used to calculate the Young's modulus of the specimen. In order to save on computation time, the rotational symmetry was exploited and only a quarter of the specimen was modelled. The test specimen was meshed with 48 hexahedral elements as

shown in Figure 6.2. This relatively rough mesh produces accurate enough results to study the behaviour of the multiscale approach.

The specimen is perfectly round in its cross section and the material is assumed to be isotropic. Hence, an axisymmetric approach using polar coordinates would also be appropriate here. The number of macro-dimensions would then be reduced to two, as the material behaves constant for every angle $\theta$. An axisymmetric approach however was not used, since the existing code is implemented in Cartesian coordinates.

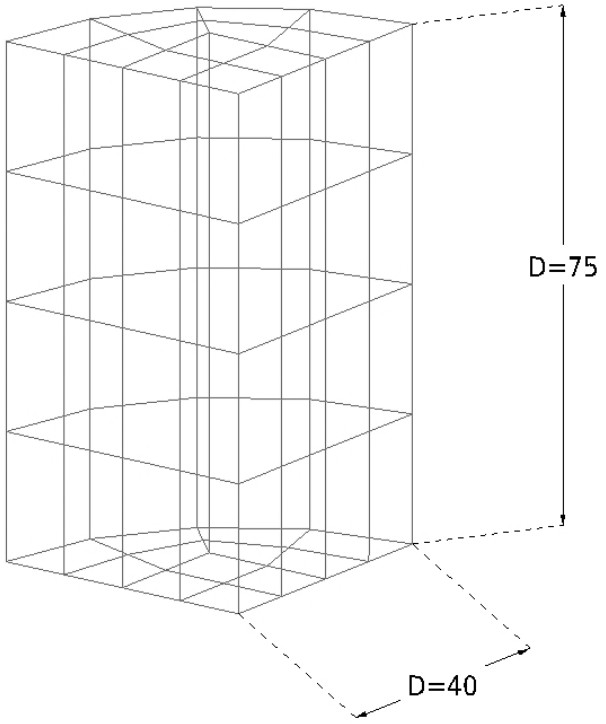


Figure 6.2: *Hexahedral Mesh*

## 6.2 Results

In the first set of simulations, the Young's modulus of the two phases was kept constant, i.e. 15 GPa for the matrix and 30 GPa for the aggregates. The internal length scale $l_{agg}$ was calculated by multiplying the aggregate size with a factor $\alpha$, according to Equation

6.2. Figure 6.3 shows the results of the experiment where different values were used for the parameter $\alpha$. It can be seen that size scale effects were captured in all the calculations.

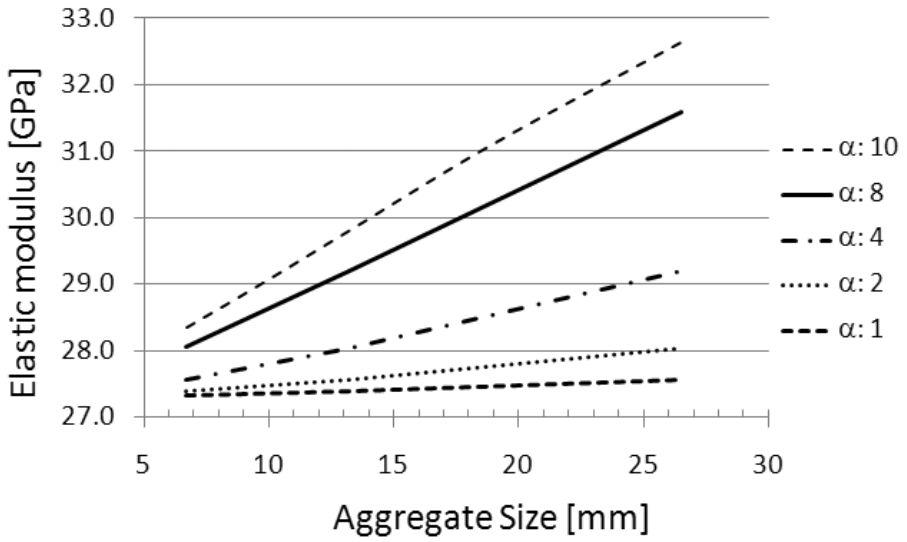


Figure 6.3: *Variation of the Elastic Moduli by Changing Aggregate Sizes and the Influence of the Scaling Parameter* $\alpha$

Furthermore, the graphs indicate that by increasing the aggregate diameter, the material stiffness generally increases. This first set of simulations illustrate how the parameter $\alpha$ affect the solution. An increase in $\alpha$ causes an increase in the slope of the size scale effects.

Figure 6.4 shows the same graphs plotted on a region where the aggregate size approaches infinitesimal small. When the aggregates become small enough, the specimen size is then larger than the RVE and a change in aggregate size should therefore no longer influence the specimen stiffness. This effect can be seen as the transition to homogeneous material behaviour. The model is in good agreement with this theoretical aspect as shown in Figure 6.4, where the graphs level out as the aggregate size approaches infinitesimally small.

In a second set of simulations, the effective Young's modulus of the aggregates $E_{agg}^{eff*}$ was varied, for a constant scaling parameter $\alpha = 8$. The Young's modulus of the matrix was again chosen to be 15 GPa. The results of calculations with four different Young's moduli in a range from 20 GPa to 35 GPa are plotted in Figure 6.5. As expected, a change in the

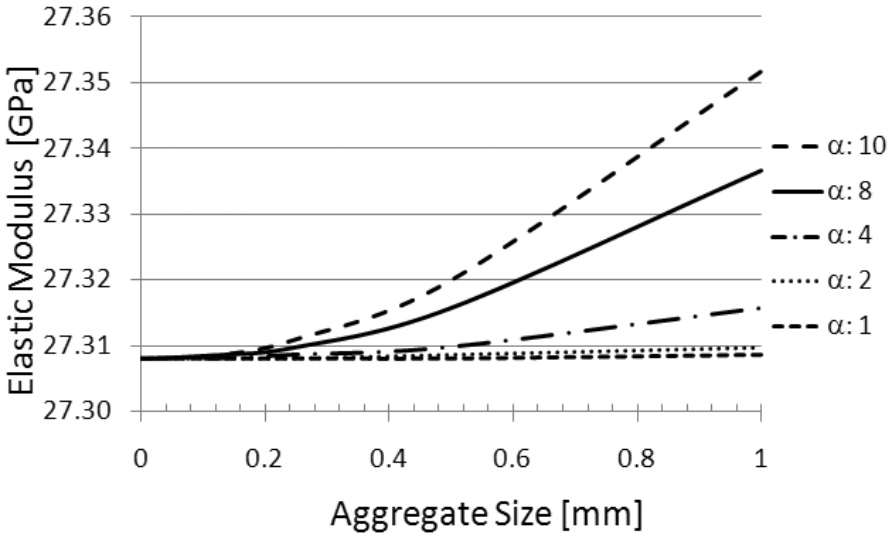


Figure 6.4: *Transition to the Classical Continuum Solution in a Region of Small Aggregate Sizes*

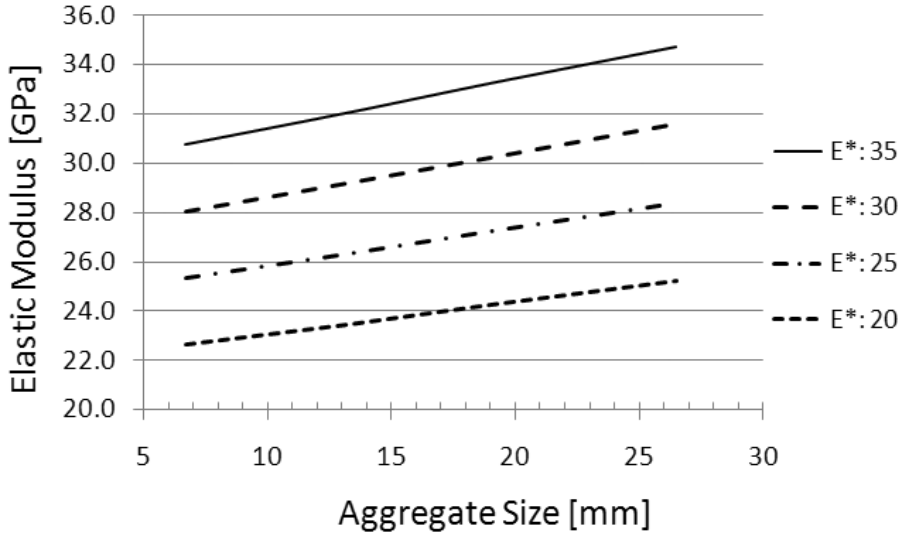


Figure 6.5: *The Effect of a Change in the Effective Aggregate Stiffness* $E_{agg}^{eff*}$

effective aggregate stiffness causes an offset on the vertical axis, while the change of the size scale effects, i.e. the graph's slope, stays constant.

## 6.3 Discussion

### 6.3.1 Effective Young's Modulus

The applied volume averaging (Eq. 6.3) is done according to the parallel model in Figure 1.1. This does not represent reality exactly, since there is no uniform strain condition in the specimen. It would be more realistic to use an average of uniform strain and uniform stress. In the uniform stress model, the overall stiffness depends mainly on the weaker phase of the composite, refer to Figure 1.2. This can be visualised by imagining aggregates embedded in a sponge where it can be easily seen that the overall Young's modulus is dominated by the stiffness of the sponge material. To achieve an overall stiffness which is between a uniform strain condition and uniform stress condition, and still using Equation 6.3, the actual aggregates stiffness needs to be reduced to $E_{agg}^{eff*}$.

### 6.3.2 Influence of the ITZ

The material was considered as a two-phase composite without taking the ITZ into consideration. The thickness of the ITZ is constant and not dependent on the size of the coarse aggregates [Hashin and Monteiro, 2002]. Due to a change in aggregate size, the volume ratio of ITZ to bulk paste changes as well. This can be explained by writing the functions of volume and surface of one aggregate

$$V_{agg} = f(d^3)\,, \tag{6.4}$$

$$S_{agg} = f(d^2)\,, \tag{6.5}$$

as well as the total number of aggregates

$$N_{agg} = f(d^{-3})\,. \tag{6.6}$$

The total volume of the ITZ can therefore be expressed with the following function

$$V_{ITZ} = h * S_{agg} * N_{agg} = f(d^{-1}) \,, \tag{6.7}$$

where $h$ is the constant thickness of the ITZ. The last function shows that the volume of the ITZ is a function of the aggregate diameter. More specifically, the ITZ volume increases by decreasing aggregate sizes.

On the one hand, since the ITZ is generally weaker than the bulk paste, the overall modulus of the composite is therefore expected to decrease with a decrease in aggregate size. On the other hand, the Young's modulus of the bulk paste is expected to be higher in a specimen with a high volume ratio of the ITZ. This can be explained due to a conservation of water; a higher water demand in the ITZ forces a lower water content in the bulk paste [Scrivener et al., 2004]. This lower water content in the bulk paste increases its stiffness which automatically increases the overall stiffness of the specimen.

It can be concluded that a change of aggregate size does not only cause a change in the internal length scale parameter, but also a change in the physical microscopical properties of the cement paste. This influence of the ITZ is yet not considered in the presented micromorphic approach.

### 6.3.3 Influence of Particle Packing

If the concrete specimens are cast in moulds, a thin surface layer will be formed with a lower volume ratio of aggregates as illustrated in Figure 6.6. This effect occurs due to the wall effect, see Figure 1.3. Due to conservation of the total volume ratio of the aggregates, the inside of the specimen is correspondingly more densely packed. The thickness of this layer is directly dependent on the diameter of the aggregates.

The influence of particle packing causes varying material behaviour between surface and interior regions of the specimen which is not considered in the current example.

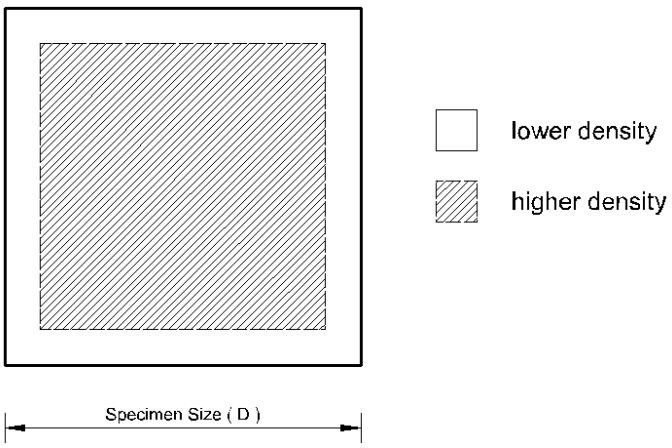


Figure 6.6: *The Effect of Particle Packing*

## 6.4 Recommendations

In the presented model size scale effects due to a change in constituent size of one phase were modelled. However, if real concrete specimens were tested, the captured results would then be a summation of different phenomena, whereas in the current approach, only the influence of non-local stress contributions is considered. Since it is unknown to what order of magnitude each phenomenon contributes to the summation of size scale effects, it would be cumbersome to verify or calibrate the presented model. To overcome this problem, another experimental approach is suggested, where the aggregate size is kept constant while the specimen size is varied. With this approach, the ratio of specimen size to internal length scale parameter is changed in the same fashion but the actual material and its microstructure is kept identical for all specimens. Furthermore, the specimen should be cut out of a larger specimen, such that the influence of particle packing can be neglected.

# Chapter 7

# Example 2

The objective of this second example is to validate the theory by means of experimental results. The aim is to reduce the influence of various size scale effects to only the non-local stress contributions. In this second example, the aggregate size is kept constant while the dimensions of the test specimens are changed. The internal length scale parameter itself is therefore not changed. The ratio between the internal length and the specimen size is, however, varied. The dimensions of the test specimens are shown in Figure 7.1, where the specimen diameter $D$ varies between 22.5 mm and 100 mm. The height of each specimen is always twice its diameter. Since the aggregate size is kept constant, the material and its microstructure is identical for all the specimens. Even though the ITZ will still exist in this approach, its influence for all specimens will be the same, regardless of the specimen size. Another improvement in this second example is that the concrete is cast in moulds and the specific specimens are cored out of larger concrete blocks. Therefore, the influence of particle packing (Section 6.3.3) and the existence of a weaker surface layer due to drying of concrete (Section 1.1.3) can be neglected. Randomness of material strength can be ignored, since the specimens are only compressed in their elastic regime, i.e. maximum load corresponding to 30% of the materials failure load.

Figure 7.2 shows the expected results qualitatively. If the specimen size is large enough compared to the aggregate size, a change in specimen size should not affect the material's Young's modulus. However, if the specimen size reaches a certain minimum threshold, size

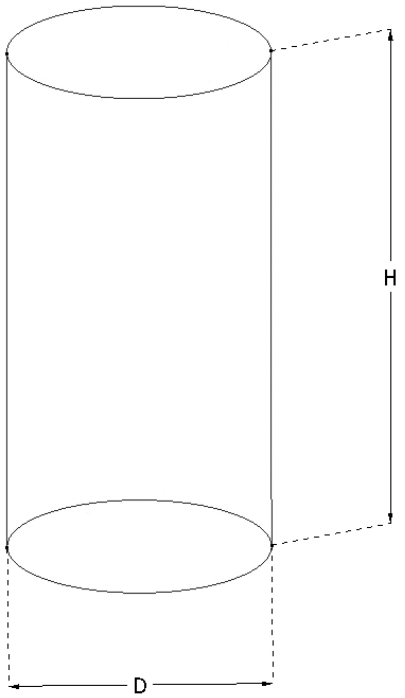


Figure 7.1: *Specimen Dimension*

effects are expected. If it is possible to obtain such a graph from the experiments, one could then infer (i) the magnitude of size scale effects in a given range of specimen to aggregate ratio and (ii) the zone where there are no longer size scale effects expected, i.e. where the criteria of the RVE is given.

A second objective of this example is to use the experimental data to calibrate the model. Values for parameter $\alpha$ and $E_{agg}^{eff*}$ will be elaborated so that the model outcome fits the experimental data.

## 7.1 Experimental Procedure

Cylindrical concrete samples with 5 different sizes were produced in this example. The aggregate size was kept constant for all the 5 specimen sizes. However, in order to cover a bigger range of specimen size to aggregate size ratio, two batches with different aggregate sizes were cast.

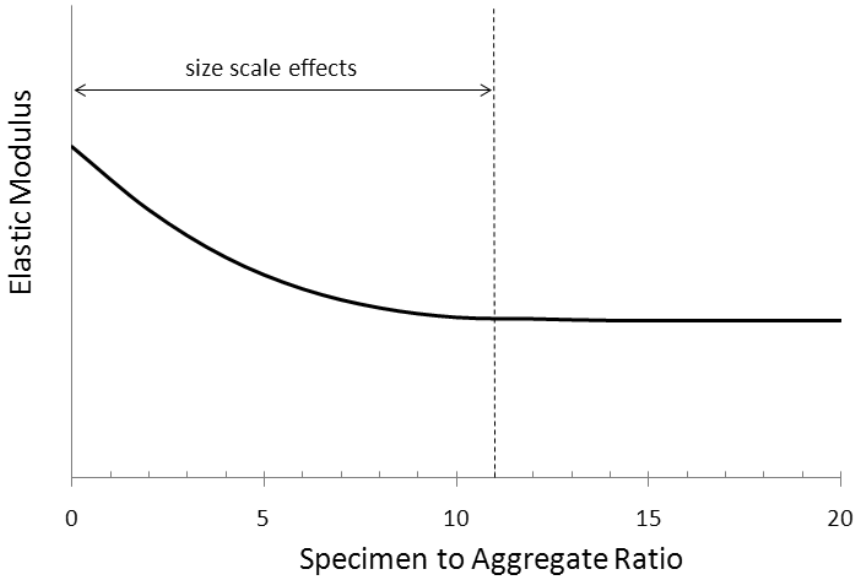


Figure 7.2: *Variation of the Elastic Moduli by Changing the Specimen to Aggregate Ratio*

### 7.1.1 Preparation of the Specimens

Specimens with the following material constituents were produced:

- Klipheuwel sand
- Fly ash (30 %)
- Ordinary Portland cement (OPC)
- Greywacke crush stone

The material and mix design used in this example are shown in Table 7.1. Two batches of concrete were produced, one with 6.7 mm stones, the other with 26.5 mm stones.

Four additional 150 mm cubes of each batch were cast for the determination of the 28 days concrete compressive strength. To obtain an indication of the matrix stiffness, specimens without stones were cast as well. The mix design of those specimens is shown in Table 7.2.

Concrete was cast in 150 mm cubical moulds. Three days after casting, the cubes were placed in a curing bath. 26 days after casting, specimens with different diameters, namely

Table 7.1: *Mix Design for Specimens per $m^3$*

| w/c [-] | Aggregate Size mm | Binder [kg] | Sand [kg] | Stone [kg] | Water [l] |
|---|---|---|---|---|---|
| 0.5 | 6.7 | 360 | 734.81 | 1072.0 | 180 |
| | 26.5 | 360 | 734.81 | 1072.0 | 180 |

Table 7.2: *Mix design for 2 Moulds (10 l mortar)*

| Cement [kg] | Fly Ash [kg] | Sand [kg] | Water [l] |
|---|---|---|---|
| 4.2 | 1.8 | 12.25 | 2.45 |

22.5, 33, 42, 68mm were cored out of the cubes, see Figure 7.3. Four specimens of each size were produced, each cored out from different concrete cube. Note that the largest specimens, i.e. 100 mm diameter, were cast and cored out of 150 mm cylinders with a height of 300 mm as shown in Figure 7.4.

The height of the specimens was cut to be exactly twice its diameter, see Figure 7.5. In order to create a flat top and bottom surface, the specimens were ground using a wet steel rotating grinder, shown in Figure 7.6.

Finally, specimens with 5 different sizes are presented in Figure 7.7.

### 7.1.2 Determination of Mean Stone Diameter

In order to determine a value for the internal length scale parameter, the mean diameter of the aggregates is needed. Note that the specification from the quarry, for example 26.5 mm aggregates, provide only a rough indication on the aggregate size. 26.5 mm aggregates include all stones of arbitrary shape which fall through a sieve with square openings of 26.5 mm and do not fall through the next smaller sieve, i.e. 19 mm. As a first step in the determination of the mean diameter, the specific weight of aggregates was determined by

Figure 7.3: *Coring a Specimen out of a 150 mm Concrete Cube*

Figure 7.4: *The 100 mm Specimens were Cored out of a 150 mm Cylinder*

Figure 7.5: *Slicing Specimen to a Height of Twice its Diameter*

Figure 7.6: *Grinding a Flat Surface of the Specimen*

measuring the weight and volume of a few aggregates. Dividing the weight of the stones over its volume led to a specific weight of $2590 kg/m^3$. In the second step, 200 of the 26.5 mm aggregates were measured while 300 of the 6.7 mm aggregates were measured. The averaged volume of a single aggregate was then determined. The mean diameter of the aggregates was calculated approximating the aggregates as perfect spheres with a volume of

$$V = \frac{4}{3} * \pi * \left(\frac{d}{2}\right)^3 \tag{7.1}$$

where $d$ represents the diameter of one aggregate.

Figure 7.7: *Specimens with 5 Different Sizes; Diameter = 100 mm, 68 mm, 42 mm, 33 mm and 22.5 mm*

The measured and the calculated values are presented in Table 7.4 in Section 7.3.

### 7.1.3 Reduction of Aggregate Diameter

Due to coring and the cutting of the specimen, the average aggregate size $d$ is subsequently reduced. This reduction has to be taken into consideration since the ratio of cut aggregates is higher in smaller specimen. The total number of aggregates is therefore higher in a specimen with cut aggregates compared to a moulded specimen where there are no cut aggregates, given that the volume ratio of aggregates is the same in both cases. A formula for the total number of aggregates in a specimen is derived, and then solved for the mean diameter of the containing aggregates.

As shown in Figure 7.8, the cross section of a specimen is divided into two parts, namely $A_1$ and $A_2$. Inside the area $A_1$, the aggregates remain undamaged after coring and cutting, whereas area $A_2$ on the border, is left damaged.

The thickness of this surface layer is in this simplified approach assumed to be half the aggregate size. Given that the volume fraction of aggregates is constant throughout the material, the relative number of aggregates in the surface area $A_2$ is twice as high as the inside area $A_1$.

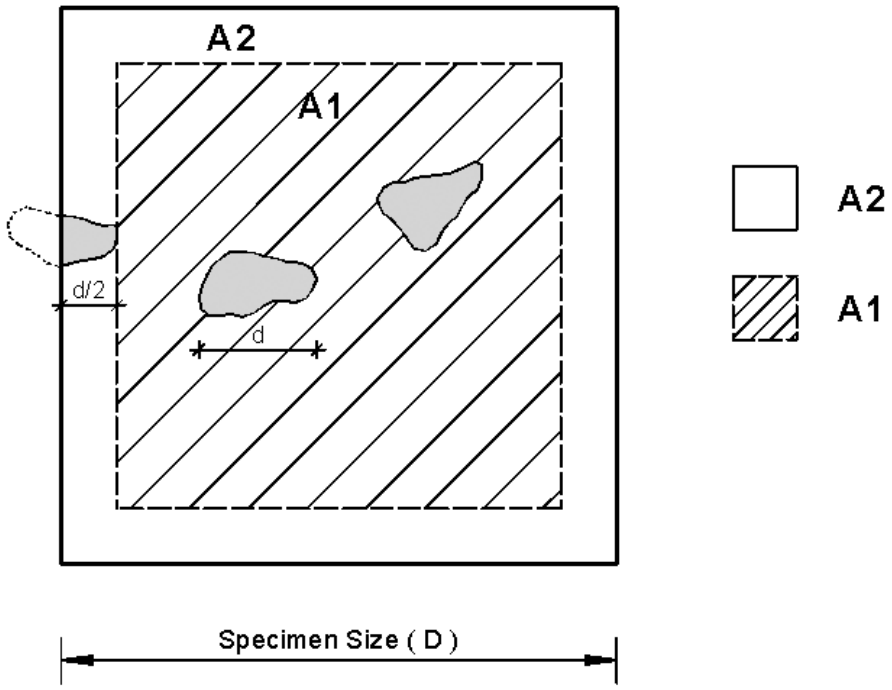


Figure 7.8: *Cross Section of a Specimen*

In the second step, the approach is extended to the three dimensional case where the two parts are volumes denoted by $V_1$ and $V_2$. Using the same principles, the formula for the total reduced number of aggregates in one specimen then becomes

$$n_r = n * \frac{V_1 + 2 * V_2}{V_1 + V_2}, \tag{7.2}$$

where the initial number of aggregates, assuming none to be cut, is given by dividing the total aggregate volume over the volume of a single aggregate

$$n = \frac{V_1 + V_2}{V_{single}}. \tag{7.3}$$

If $D$ represents the specimen diameter, $H$ the specimen height and considering a volume fraction of 0.4, the two volumes are then given as

$$V_1 = 0.4 * \left(\frac{D-d}{2}\right)^2 * \pi * (H-d) \qquad \text{and} \qquad V_2 = 0.4 * \left(\frac{D}{2}\right)^2 * \pi * H - V_1. \tag{7.4}$$

Knowing the actual number of aggregates in a specimen, the volume of a single aggregate is obtained by

$$V_{single,r} = \frac{V_1 + V_2}{n_r}. \tag{7.5}$$

Finally, the reduced mean diameter of the aggregates in the specific specimen is then obtained using Equation 7.1

$$d_r = 2 * \left( \frac{V_{single,r} * 3}{4 * \pi} \right)^{\frac{1}{3}}. \tag{7.6}$$

For computing the internal length scale parameter and for the presentation of the results, the reduced mean diameter $d_r$ is used.

Since the aggregates are randomly packed in concrete, the assumptions made in this approach only hold true if an infinitely large number of samples are considered. However, even if there are only a few specimens tested, it can still be seen as a good approximation.

### 7.1.4 Determination of the Compressive Strength

Three 150 mm concrete cubes of each batch were tested for the 28 day compressive strength. The dimensions of each specimen were measured after the surface water from the curing bath was removed. The samples, in a saturated condition, were then placed centrally between the parallel flat steel platens of a compression testing machine as shown in Figure 7.9. The cubes were positioned so that the load was applied to the side faces of the cubes, i.e. parallel to the direction of casting. The load was continuously increased with a constant rate of $0.3N/(mm^2s) \pm 0.1N/(mm^2s)$ until the cube failed, i.e. until no greater load could be sustained by the specimen. The failure load and the dimensions of each specimen were monitored and the concrete compressive strength was calculated according to Equation 2.1. The average strength $f_c$ of the three cubes, rounded to the nearest $0.5N/mm^2$, was the result used for the further procedure of this example. This testing procedure is in accordance with the South African Standards [SANS5863, 2006].

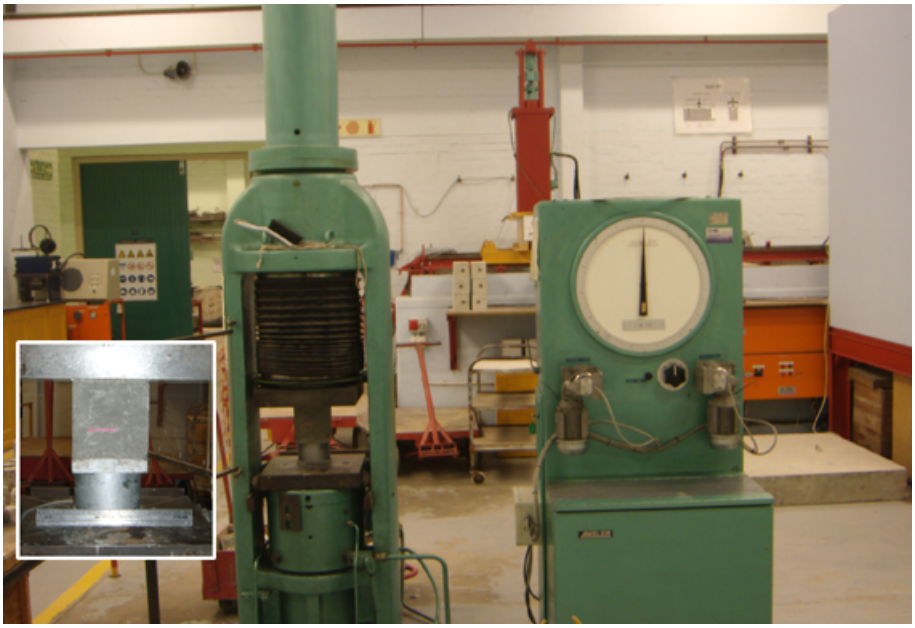

Figure 7.9: *Compression Testing Machine*

### 7.1.5 Determination of the Young's Modulus

The Young's Modulus was obtained by compressing the specimens in a Zwick Roell compression machine and measuring their deformation using a target gun extensometer. The targets were attached on two opposite sides of each specimen. The gauge length is not less than two-thirds of the diameter of the cylinder and the distance from its ends is not less than one-quarter of the height of the test specimen. All prepared test specimens had any surface water removed and were tested in a moist condition. The specimens were placed centrally between the parallel flat steel platens of the Zwick Roell machine. As the exact parallelism of the cylinder surfaces could not entirely be ensured, a swivel head was placed in between the specimen and the upper steel platen of the machine as shown in Figure 7.10. A swivel head ensures that the specimen is compressed uniformly, even if its upper and lower surfaces are not exactly parallel. Four samples of each specimen size and each aggregate size were tested.

Firstly, each specimen was compressed twice up to a maximum stress corresponding to 30 % of the determined 28-day compressive strength, while the load was removed completely after each loading cycle. During the third loading cycle, strain measurements were taken at


Figure 7.10: *Specimen Being Tested on a Zwick Roell Machine*

a stress $\sigma_a = 0.1 f_c$ and a stress $\sigma_b = 0.3 f_c$. The load in all three loading cycles was applied constantly with a rate within the range $0.6N/(mm^2 s) \pm 0.4N/(mm^2 s)$. The test setup and how the strain measurements were taken for specimens with different sizes is shown in Figure 7.11 and 7.12.

Figure 7.11: *Strain Measurement on the Smallest Specimen*

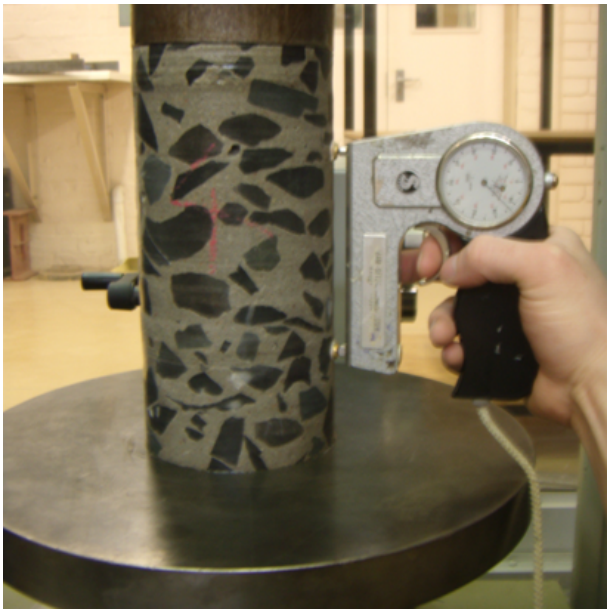

Figure 7.12: *Strain Measurement on the Largest Specimen*

The static modulus of elasticity in compression $E_c$ is then given by the formula

$$E_c = \frac{\sigma_b - \sigma_a}{\triangle\varepsilon}. \tag{7.7}$$

This testing procedure was modified from the British Standard [BS1881:Part121, 1983]. The British Standard specifies the minimum dimension for specimen to not be less than three times the nominal maximum size of aggregate nor less than 100 mm diameter. These specifications however were ignored, since the purpose of this example was to capture size scale effects.

## 7.2 Simulations

For modelling purposes, the material is also considered as a two-phase composite consisting of aggregates embedded in a mortar matrix. Table 7.3 displays the material properties used in the model. Since the concrete was only compressed to one-third of its failure load, the material behaviour can be considered as linear elastic. The classical *St. Venant-Kirchhoff* model was therefore chosen, however applied to the extended tensor space in order to accommodate the generalised *Cauchy-Green* deformation tensor $\tilde{\mathbf{C}} \in \mathbb{E}^4 \otimes \mathbb{E}^4$. More detailed information on how the constitutive realtion was computed can be found in Section 4.3. The

Table 7.3: *Constitutive Parameters*

| | Unit | Aggregates$_{6.7mm}$ | Aggregates$_{26.5mm}$ | Matrix |
|---|---|---|---|---|
| $E^*$ | [GPa] | 25 | 25 | 22.2 |
| $\nu^*$ | [-] | 0.2 | 0.2 | 0.2 |
| $\alpha$ | [mm] | 70 | 16 | - |
| $c_1$ | [GPa] | 16.67 | 16.67 | 24.67 |
| $c_2$ | [GPa] | 41.67 | 41.67 | 37.0 |
| $n$ | [%] | 40 | 40 | 60 |

micro-directors in the undeformed configuration are assumed to be parallel to the applied

load. Again, the calculations were performed in a displacement control mode. The displacements on the bottom plane of the cylindrical specimen are fixed in all three axes. On the top plane only the tangential displacements components are fixed and the component parallel to the cylinder axis was set to 1 mm. The lateral constraint is due to friction between the compression platens and the specimen surface.

The internal length $l^I$ was chosen to be 1 for the matrix and computed according to Equation 6.2 for the aggregates. Note that for the calculation of the internal length of the aggregate, the reduced aggregate diameter $d_r$ was used (see Table 7.5). The parameter $\alpha$ was chosen such that the slope of the results matches the experimental results. Also, the effective Young's modulus of the aggregates $E_{agg}^{eff*}$ was chosen to fit the experimental results.

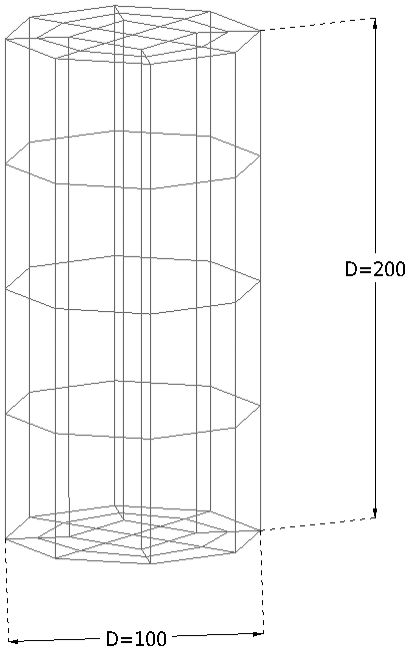


Figure 7.13: *Mesh of the 100 mm Specimen*

Figure 7.13 shows the mesh of the 100 mm specimen. It is constructed with 80 hexahedral elements. The number of elements was chosen to be the same for all the specimens, so that the accuracy of the results is for all the specimens identical.

## 7.3 Results

### 7.3.1 Aggregate Diameter

The mean volume of each aggregate size was determined (Equation 7.1) and its corresponding mean diameter calculated approximating the aggregates as perfect spheres (Equation 7.6). The obtained values for the mean diameter can be found in Table 7.4. Note that the mean aggregate diameter are around 15 % lower than the aggregate specification.

Table 7.4: *Determination of Mean Aggregate Diameter*

| Aggregate [mm] | Number [-] | Mass [kg] | Total Volume [mm$^3$] | Mean Volume [mm$^3$] | Mean Diameter [mm] |
|---|---|---|---|---|---|
| 26.5 | 200 | 3.215 | 1.24e+6 | 6.21e+3 | 22.8 |
| 6.7 | 300 | 0.075 | 2.9e+4 | 9.65e+1 | 5.7 |

The reduced aggregate diameter and the ratio of the specimen diameter $D$ to aggregate diameter $d_r$ was computed according to Subsection 7.1.3. Table 7.5 shows the values of the reduced aggregate diameter of each specimen size and the corresponding ratio of aggregate to specimen.

### 7.3.2 Compressive Strength

Measurements and results of the 28-day compressive strength of the 150 mm cubes are presented in Table 7.6 and 7.7. These values are used to determine the maximum compressive stress applied ($\sigma_b = 0.3 f_c$) for the determination of the Young's modulus.

### 7.3.3 Young's Modulus

The experimental results as well as the predicted values using the outlined model are presented in Figure 7.14 for the first batch with 6.7 mm aggregates and in Figure 7.15 for the

Table 7.5: *Reduced Aggregate Diameter and Specimen to Aggregate Ratio*

| Aggregate [-] | Mean Diameter [mm] | Specimen Size $D$ [mm] | Reduced Diameter $d_r$ [mm] | $D$ / $d_r$ Ratio [-] |
|---|---|---|---|---|
| 26.5 | 22.8 | 22.5 | 18.1 | 1.2 |
| | | 33 | 18.3 | 1.8 |
| | | 42 | 18.6 | 2.3 |
| | | 68 | 19.4 | 3.5 |
| | | 100 | 20.0 | 5.0 |
| 6.7 | 5.7 | 22.5 | 5.0 | 4.5 |
| | | 33 | 5.1 | 6.4 |
| | | 42 | 5.2 | 8.0 |
| | | 68 | 5.4 | 12.7 |
| | | 100 | 5.5 | 18.3 |

Table 7.6: *Determination of Compressive Strength - Measurements*

| Aggregate [mm] | Number [-] | Mass [kg] | Height [mm] | Failure Load [kN] |
|---|---|---|---|---|
| 26.5 | 1 | 8.010 | 149 | 762 |
| | 2 | 8.130 | 150 | 754 |
| | 3 | 8.185 | 151 | 696 |
| 6.7 | 1 | 8.005 | 148 | 820 |
| | 2 | 8.035 | 148 | 790 |
| | 3 | 8.215 | 151 | 776 |

second batch with 26.5 mm aggregates.

Judging by the outcome of the experiments it can clearly be seen that (i) size scale effects were captured in this specific example and (ii) by decreasing the aggregate diameter, the material stiffness increases. The Young's modulus of the smallest specimen, i.e. core diameter of 33 mm, is approximately 25 % higher in both batches than in the largest specimen. Note

Table 7.7: *Determination of Compressive Strength - Results*

| Aggregate [mm] | Density [kg/m$^3$] | Compressive Strength [N/mm$^2$] |
|---|---|---|
| 26.5 | 2402.5 | 33.0 |
| 6.7 | 2411.5 | 35.5 |

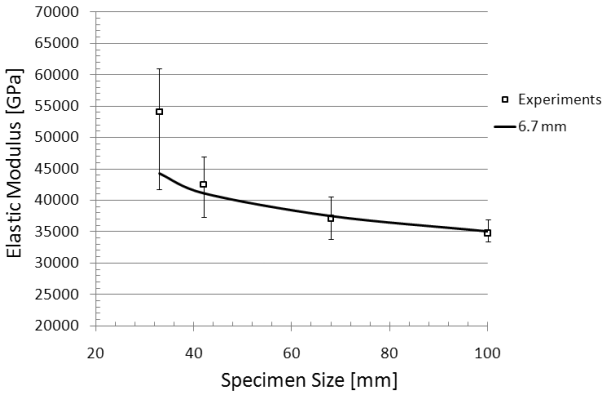


Figure 7.14: *Variation of the Elastic Modulus by Changing Specimen Size - 6.7 mm Aggregates*

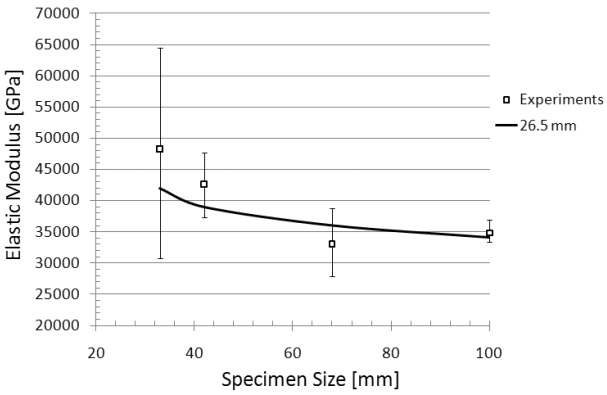


Figure 7.15: *Variation of the Elastic Modulus by Changing Specimen Size - 26.5 mm Aggregates*

that the standard deviation of the experimental results increases in the smaller specimen. Due to this observation, it was decided that the tests on the 22.5 mm specimen should not be carried out. Generally, the standard deviation on the obtained experimental results is high. Observation and conclusions therefore have to be drawn carefully.

The model could predict similar trends as observed in (i) and (ii). Furthermore, it was possible to achieve the same results according to a best fit of the experimental results by choosing the material parameters presented in Table 7.3. As learnt in example one, the parameter $\alpha$ was chosen such that the slope of the curve matches the experiments. Likewise, the effective aggregate stiffness $E_{agg}^{eff*}$ was elaborated such that the horizontal offset of the curve fits with the experiments. Recall that the slope of the curve represents the magnitude of the size scale effects and the horizontal offset represents the overall stiffness of the specimen.

### 7.3.4 Result Verification

To verify the obtained experimental results, the values are compared with three theoretical approaches to predict the Young's modulus of concrete. A very simple check of the results is to use Equation 1.1, where the Young's modulus is correlated with the compressive strength of concrete. Alexander and Beushausen [2009] specify that $K_0 = 24GPa$ and $\alpha = 0.25$ be used for the aggregate type used in this concrete.

The series and parallel model represent a theoretical upper and lower bound. The Young's modulus of the cement matrix is $29.2GPa$ which was obtained in the experiments. The Young's modulus of the aggregates is taken to be $72GPa$. Note, these two models are conservative assumptions, since they do not take the ITZ nor the aggregate size into account.

Table 7.8: *Theoretical Predictions of Young's Moduli*

| Model | 6.7 mm | 26.5 mm |
|---|---|---|
| | [GPa] | [GPa] |
| $E_{c,28}$ | 32.9 | 32.3 |
| Series Model | 38.3 | 38.3 |
| Parallel Model | 46.3 | 46.3 |

The predictions of the Young's moduli for the concrete used in the experiments are presented in Table 7.8. All those models assume that the RVE is given and therefore do not account for size effects. Hence, these predictions are compared with largest specimen, i.e. a core of 100 mm. The $35GPa$ obtained for the largest specimens agree well with the theoretical predictions.

## 7.4 Discussion

The obtained experimental results confirmed the expected trend, i.e. the stiffness of the material increases when the specimen size decreases. Specimens with smaller aggregates subsequently have a higher specimen to aggregate ratio, which makes them less prone to size effects. When this ratio becomes large, no size scale effects are expected, i.e. a change in specimen size should no longer affect the Young's modulus, refer to Figure 7.2. Figure 7.16 shows the experimental and modelling results with respect to the ratio of specimen to aggregate size. It can be observed in both the model and the experiments that as the ratio increases, the size effects decrease. Based on the limited range of specimen sizes, a firm transition zone to where no size effect could unfortunately not be observed in the current example.

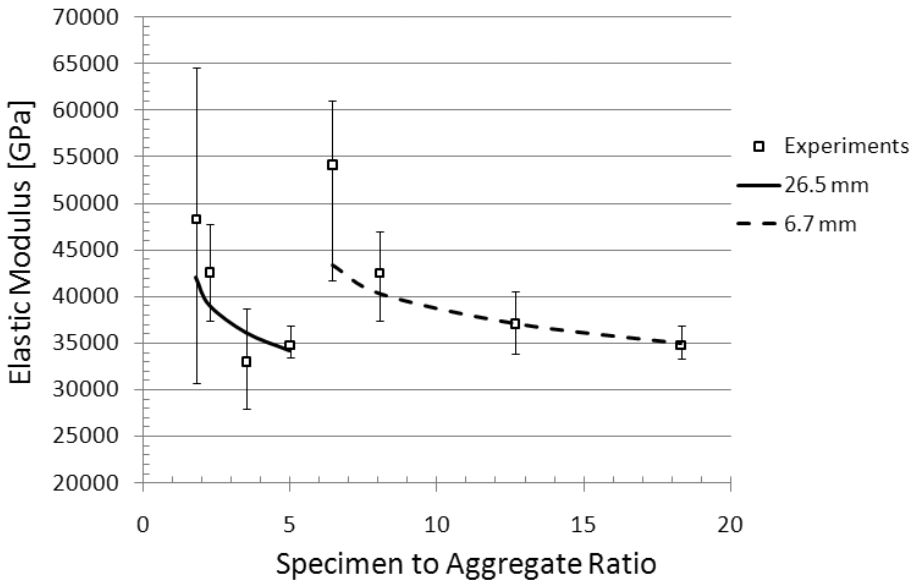


Figure 7.16: *The Effect of a Change in the Effective Aggregate Stiffness* $E_{agg}^{eff*}$

Note that observations and conclusions based on the experimental data have to be drawn carefully, since each obtained Young's modulus is only taken from the average of four samples. To obtain more accurate results, further experiments have to be carried out with a higher number of samples. The relative error in strain readings is the same for all the specimens. Since the gauge length in small specimens is less than in large specimens, the absolute error

is larger in the small specimens and hence, their Young's moduli varies more. This explains, from a measurement point of view, the higher standard deviation in the smaller specimens. From a material point of view, the concrete in small specimens is more heterogeneous. In essence, the exact volume ratio of specimens may vary from specimen to specimen. The accuracy of the stress reading is limited by the accuracy of the relevant testing machine.

This limitations could be overcome by (i) testing a higher range of specimen sizes and (ii) testing more samples of each size which should provide a better statistical average.

The accuracy of the computer simulations is limited by the choice of quadrature order and mesh fineness. The quadrature order, number of elements and the element structure of each specimen was chosen to be equal. This ensures that the accuracy of the Young's modulus is not dependent on the specimen size which can be proved by comparing the exact solution, given as

$$E = \frac{\sigma}{\varepsilon} = \frac{\frac{F}{A}}{\frac{\Delta H}{H}}\,, \tag{7.8}$$

and the modelled solution denoted with a subscript $h$ given as

$$E^h = \frac{\sigma^h}{\varepsilon} = \frac{\frac{F^h}{A^h}}{\frac{\Delta H}{H}}. \tag{7.9}$$

The displacement $\Delta H$ and the height of a specimen $H$ is given in a displacement control calculation and can therefore be seen as exact. The area of applied load $A^h$ is approximated with straight lines and therefore directly dependent on the element number. As the element number is the same for all specimens, the relative error is also the same for all specimens. Hence, since the applied stress is constant for all the specimens, the error is size independent.

# Chapter 8

# Conclusion and Recommendations

## 8.1 Conclusion

A micromorphic continuum theory with multiple micro-spaces is outlined and successfully implemented. For the modelling of concrete specimens under uniaxial compression, two micros-spaces are attached to every macro material point which represent the aggregates and the cement matrix. In the current approach, the micro-spaces are represented by one-dimensional micro-directors which which describe two independent micro-displacement fields. By adding non-local information to governing and constitutive equations, the material's micro-structure is taken into account on kinematics level. Since the magnitude of the micro-displacement field refers to an internal length scale, micromorphic formulations can describe elastic size-scale effects in concrete specimens. The theory states that if the aggregate size is increased, or the specimen size decreased, the overall Young's modulus of the specimen becomes larger. This size-scale phenomenon could be captured with the implemented model. Furthermore, experiments could confirm this trend as well. However, the experimental results are not consistent enough to draw complete quantitative conclusions.

In order to apply this model in practice, i.e. estimating Young's modulus and size scale effects for a specific concrete specimen further work needs to be done. Many more experimental data, with a variety of different materials and a large range of specimen sizes,

must be captured and analysed to establish the link between conventional and micromorphic model parameters.

## 8.2 Recommendations

In order to precisely estimate the Young's modulus of two phase composites, predicting when size effects occur and what magnitude the size effects will be, further investiagtions need to be carried out. On the one hand, the implemented model can be improved and on the other hand, more experimental data need to be captured.

Currently, only straightforward volume averaging of the two phases is considered to obtain the overall Young's modulus of concrete. To achieve meaningful results, the effective stiffness of the aggregates needs to be reduced. This produces an unknown factor which can only be found out through experimentation. To overcome this problem, the code should be modified using Hirsch's model (see Figure 1.1), which is an average of uniform strain and uniform stress conditions. Using Hirsch's model, it should be possible to obtain an accurate estimation of the overall Young's modulus without reducing the aggregate stiffness. The model could also be extended by incoorporating a third micro-space. Having a third micro-space, the material could then be considered as a three phase continuum, consisting of aggregates, interfacial transition zone and cement matrix. As a final improvement, it is suggested that the dimension of the micro-spaces is extended from one to three. This would simplify the geometrical approximation of the material's micro-structure.

The link between conventional and micromorphic model parameters needs to be established by analysing a large variety of experimental data. Experiments should be carried out with different matrix materials as well as different geometries, shapes and volume fractions of the aggregates. A starting point for experimental testing could be glass-epoxy composite with spherical inclusions. This may reduce the many unknown factors inherent in concrete specimens, since spherical aggregates are identical to one another and the epoxy matrix does not form an ITZ. Lastly, the experiments should include a larger range of specimen sizes or aggregate diameters in order to cover a large range of the specimen size to aggregate ratio.

# Bibliography


Brian Addis.

*Fundamentals of Concrete*.

Cement & Concrete Institute, South Africa, 2007.

E.C. Aifantis.

Strain gradient interpretation of size effects.

*International Journal of Fracture*, 95:299–314, 1999.

Mark Alexander and Hans Beushausen.

*Fulton's concrete technology*, chapter Deformation and volume change of hardened concrete, pages 111–154.

Cement & Concrete Institute, 2009.

M.G. Alexander.

*Fulton's concrete technology*, chapter Deformation and volume change of hardened concrete, pages 107–152.

Portland Cement Institute, 1994.

G. Altay and M. Cengiz Dökmeci.

A polar theory for vibrations of thin elastic shells.

*Innternational Journal of Solids and Structures*, 43:2578–2601, 2006.

I. Babuška and J.M. Melenk.

The partition of unity method: Basic theory and applications.

*International Journal for Numerical Methods in Engineering*, 40:727–758, 1997.

Z.P. Bažant, M. Jirásek, and R. Gettu.

Rilem tc qfs 'quasibrittle fracture scaling and size effect' - final report.

*Materials and Structures*, 37:547–568, 2004.

T. Belytschko and T. Black.

Elastic crack growth in finite elements with minimal remeshing.

*International Journal for Numerical Methods in Engineering*, 45:607–620, 1999.

T. Belytschko, L. Gu, and Y.Y. Lu.

Fracture and crack growth by element-free galerkin methods.

*Modelling and Simulation in Materials Science and Engineering*, 2:519–534, 1994a.

T. Belytschko, Y.Y. Lu, and L. Gu.

Element-free galerkin methods.

*International Journal for Numerical Methods in Engineering*, 37:229–256, 1994b.

T. Belytschko, Y. Krongauz, D. Organ, M. Fleming, and P. Krysl.

Meshless methods: An overview and recent developments.

*Computer Methods in Applied Mechanics and Engineering*, 139:3–47, 1996.

Stéphane Bordas and Marc Duflot.

Derivative recovery and a posteriori error estimate for extended finite elements.

*Computational Methods for Applied Mechanics in Engineering*, 196:3381–3399, 2007.

BS1881:Part121.

*Testing concrete - Part 121. Method for determination of static modulus of elasticity in compression.*

British Standards Institution, 1983.

Y. Choquet-Bruhat, C. DeWitt-Morette, and M. Dillard-Bleick.

*Analysis, Manifolds and Physics Part I.*

North-Holland, Amsterdam, 1982.

T. Dillard, S. Forest, and P. Ienny.

Micromorphic continuum modelling of the deformation and fracture behaviour of nickel foams.

*European Journal of Mechanics A/Solids*, 25:526–549, 2006.

John Dolbow and Ted Belytschko.

An introduction to programming the meshless element free galerkin method.

*Archives in Computational Mechanics*, 5:207–241, 1998.

W.J. Drugan and J.R. Willis.

A micromechanics-based nonlocal constitutive equation and estimates of representative volume element size for elastic composites.

*J. Mech. Phys. Solids*, 44:497–524, 1996.

C.A. Duarte and J.T. Oden.

Hp clouds - a hp meshless method.

*Numerical Methods for Partial Differential Equations*, 12:673–705, 1996.

U. Engel and R. Eckstein.

Microforming - from basic research to its realization.

*Journal of Materials Processing Technology*, 125-126(125-126):35–44, 2002.

J.L. Ericksen and C. Truesdell.

Exact theory of stress and strain in rods and shells.

*Archive for Rational Mechanics and Analysis*, 1:295–323, 1957.

A. C. Eringen.

On nonlocal plasticity.

*International Journal of Engineering Science*, 19:1461–1474, 1981.

A. C. Eringen and D. G. B. Edelen.

On nonlocal elasticity.

*International Journal of Engineering Science*, 10:233–248, 1972.

A.C. Eringen.

*Continuum Physics II.*

Academic Press, New York, 1975.

A.C. Eringen.

*Microcontinuum field theories I: Foundations and Solids.*

Springer, New York, 1999.

N.A. Fleck and J.W. Hutchinson.

A reformulation of strain gradient plasticity.

*Journal of Mechanics and Physics of Solids*, 49:2245–2271, 2001.

R.A. Gingold and J.J. Monaghan.

Smoothed particle hydrodynamics: theory and application to non-spherical stars.

*Monthly Notices of the Royal Astronomical Society*, 181:375–389, 1977.

Z. Hashin and P.J.M. Monteiro.

An inverse method to determine the elastic properties of the interphase between the aggregate and the cement paste.

*Cement and Concrete Research*, 32:1291–1300, 2002.

T.J.R Hughes.

*The Finite Element Method: Linear Static and Dynamic Finite Element Analysis.*

Dover, 2000.

X. Lai, L. Peng, P. Hu, S. Lan, and J. Ni.

Material behavior modelling in micro/meso-scale forming process with considering size/scale effects.

*Computational Materials Science*, 43:1003–1009, 2008.

D.C.C. Lam, F. Yang, A.C.M Chong, J. Wang, and P. Tong.

Experiments and theory in strain gradient elasticity.

*Journal of the Mechanics and Physics of Solids*, 51:1477–1508, 2003.

D. Leşan and R. Quintanilla.

Thermal stresses in microstretch elastic plates.

*International Journal of Engineering Science*, 43:885–907, 2005.

J. D. Lee and Y. Chen.

Electromagnetic wave propagation in micromorphic elastic solids.

*International Journal of Engineering Science*, 42:841–848, 2004.

K.M. Lee and J.H. Park.

A numerical model for elastic modulus of concrete considering interfacial transistion zone.

*Cement and Concrete Research*, 38:396–402, 2008.

J. Lemaitre.

*Continuum Damage Mechanics; Teory and Applications*, chapter Formulation and Identification of Damage Kinetic Constitutive Equations, pages 37–89.

Springer - Verlag Wien - New York, 1987.

L.B. Lucy.

A numerical approach to the testing of the fission hypothesis.

*The astronomical journal*, 82(12):1013–1024, 1977.

Melanie P. Lutz, Paulo J.M. Monteiro, and Robert W. Zimmmerman.

Inhomogeneous interfacial transistion zone model for the bulk modulus of mortar.

*Cement and Concrete Research*, 27:1113–1122, 1997.

S. Mahabunphachai and M. Koç.

Investigation of size effects on material behavior of thin sheet metals using hydraulic bulge testing at micro/meso-scales.

*International Journal of Machine Tools and Manufacture*, 48:1014–1029, 2008.

G. Thomas Mase and George E. Mase.

*Continuum Mechanics for Engineers.*

CRC Press, 1999.

C. McVeigh and W.K. Liu.

Linking microstructure and properties through a predictive multiresolution continuum.

*Computer Methods in Applied Mechanics and Engineering*, 197:3268–3290, 2008.

J.F. Michel and P. Picart.

Size effects on the constitutive behaviour for brass in sheet metal forming.
*Journal of Materials Processing Technology*, 141:439–446, 2003.

R.D. Mindlin.
Micro-structure in linear elasticity.
*Archive for Rational Mechanics and Analysis*, 16:51–78, 1964.

Nicolas Moës, John Dolbow, and Ted Belytschko.
A finite element method for crack growth without remeshing.
*International Journal for Numerical Methods in Engineering*, 46:131–150, 1999.

A. Ian Murdoch.
*The Rational Spirit in Modern Continuum Mechanics*, chapter On the Microscopic Interpretation of Stress and Couple Stress, pages 599 – 625.
Kluwer Academic Publisher, 2004.

J.C. Nadeau.
A multiscale model for effective moduli of concrete incorporating itz water-cement ratio gradients, aggregate size distributions, and entrapped voids.
*Cement and Concrete Research*, 33:103–113, 2003.

B. Nayroles, G. Touzot, and P. Villon.
Generalizing the finite element method: Diffuse approximation and diffuse elements.
*Computational Mechanics*, 10:307–318, 1992.

V.P. Nguyen, T. Rabczuk, S. Bordas, and M. Duflot.
Meshless methods: A review and computer implementation aspects.
*Mathematics and Computers in Simulation*, 79:763–813, 2008.

Ulrik Nilsen and Paulo J.M. Monteiro.
Concrete: A three phase material.
*Cement and Concrete Research*, 23:147–151, 1993.

Gill Owens, editor.
*Fulton's concrete technology.*

Cement & Concrete Institute, 9 edition, 2009.

L. Peng, F. Liu, J. Ni, and X. Lai.

Size effects in thin sheet metal forming and its elastic-plastic constitutive model.

*Materials and Design*, 28:1731–1736, 2007.

S. Ramezani and R. Naghdabadi.

Energy pairs in the micropolar continuum.

*International Journal of Solids and Structures*, 44:4810–4818, 2007.

S. Ramezani, R. Naghdabadi, and S. Sohrabpour.

Analysis of micropolar elastic beams.

*European Journal of Mechanics A/Solids*, 28:202–208, 2009.

SANS10100-1.

*Code of practice for the structural use of concrete.*

South African Bureau of Standards, Pretoria, 2000.

SANS5862-1.

*Concrete tests - Consistence of freshly mixed concrete - Slump test.*

South African Bureau of Standards, Pretoria, 2006.

SANS5863.

*Concrete tests - Compressive strength of hardened concrete.*

South African Bureau of Standards, Pretoria, 2006.

C. Sansour.

A unified concept of elastic-viscoplastic cosserat and micromorphic continua.

*Journal de Physique IV Proceedings*, 8:341–348, 1998.

C. Sansour, S. Skatulla, and H. Zhib.

A formulation for the micromorphic continuum at finite inelastic strains.

*International Journal of Solids and Structures*, 47:1546–1554, 2010.

Karen L. Scrivener, Alison K. Crumbie, and Peter Laugesen.

The interfacial transition zone (itz) between cement paste and aggregate in concrete.
*Interface Science*, 12:411–421, 2004.

Peter Simeonov and Shuaib Ahmad.
Effect of transistion zone on the elastic behavior of cement-based composites.
*Cement and Concrete Research*, 25:165–176, 1995.

Sebastian Skatulla.
*Computational aspects of generalized continua based on moving least square approximations.*
PhD thesis, University of Adelaide, September 2006.

Zhihui Sun, Edward J. Garboczi, and Surendra P. Shah.
Modeling the elastic properties of concrete composites: Experiment, differential effective medium theory, and numerical simulation.
*Cement & Concrete Composites*, 29:22–38, 2007.

J.G.M. van Mier and M.R.A. van Vliet.
Influence of microstructure of concrete on size/scale effects in tensile fracture.
*Engineering Fracture Mechanics*, 70:2281–2306, 2003.

M. Vořechovský.
Interplay of size effects in concrete specimens under tension studied via computational stochastic fracture mechanics.
*International Journal of Solids and Structures*, 44:2715–2731, 2007.

Geregory J. Wagner and Wing Kam Liu.
Application of essential boundary conditions in mesh-free methods: a corrected collocation method.
*International Journal for Numerical Methods in Engineering*, 47:1367–1379, 2000.

M. Wang, P.H.S.W. Kulatilake, J. Um, and J. Narvaiz.
Estimation of rev size and three-dimensional hydraulic conductivity tensor for a fractured rock mass through a single well packer test and discrete fracture fluid flow modeling.

*International Journal of Rock Mechanics & Mining Sciences*, 39:887–904, 2002.

Z.C. Xia and J.W. Hutchinson.

Crack tip fields in strain gradient plasticity.

*Journal of the Mechanics and Physics of Solids*, 10:1621–1648, 1996.

X. Frank Xu and Xi Chen.

Stochastic homogenization of random elastic mulit-phase composites and size quantification of representative volume element.

*Mechanics of Materials*, 41:174–186, 2009.

A. Zervos, P. Papanastasiou, and I. Vardoulakis.

Modelling of localization and scale effect in thick-walled cylinders with gradient elastoplasticity.

*International Journal of Solids and Structures*, 38:5081–5095, 2001.

Xing-Hua Zhao and W.F. Chen.

Effective elastic moduli of concrete with interface layer.

*Computers & Structures*, 66:275–288, 1998.

O.C. Zienkiewicz and R.L. Taylor.

*The Finite Element Method for Solid and Structural Mechanics.*

Elsevier, 2005.